MOX-Report No. 08/2022

Reduced order modeling of nonlinear microstructures through Proper Orthogonal Decomposition

Gobat, G.; Opreni, A.; Fresca, S.; Manzoni, A.; Frangi, A.

MOX, Dipartimento di Matematica
Politecnico di Milano, Via Bonardi 9 - 20133 Milano (Italy)

mox-dmat@polimi.it http://mox.polimi.it

Reduced order modeling of nonlinear microstructures through Proper Orthogonal Decomposition

Giorgio Gobat[1], Andrea Opreni[1], Stefania Fresca[2], Andrea Manzoni[2], and Attilio Frangi[1]

[1]Dept. of Civil and Environmental Engineering, Politecnico di Milano, P.za Leonardo da Vinci 32, 20133 Milano, Italy*
[2]MOX - Dept. of Mathematics, Politecnico di Milano, P.za Leonardo da Vinci 32, 20133 Milano, Italy†

Abstract

We apply the Proper Orthogonal Decomposition (POD) method for the efficient simulation of several scenarios undergone by Micro-Electro-Mechanical-Systems, involving nonlinearites of geometric and electrostatic nature. The former type of nonlinearity, associated to the large displacements of the devices, leads to polynomial terms up to cubic order that are reduced through exact projection onto a low-dimensional subspace spanned by the Proper Orthogonal Modes (POMs). On the contrary, electrostatic nonlinearities are modeled resorting to precomputed manifolds in terms of the amplitudes of the electrically active POMs. We extensively test the reliability of the assumed linear trial space in challenging applications focusing on resonators, micromirrors and arches also displaying internal resonances. We discuss several options to generate the matrix of snapshots using both classical time marching schemes and more advanced Harmonic Balance (HB) approaches. Furthermore, we propose a comparison between the periodic orbits computed with POD and the invariant manifold approximated with Direct Normal Form approaches, further stressing the reliability of the technique and its remarkable predictive capabilities, e.g., in terms of estimation of the frequency response function of selected output quantities of interest.

1 Introduction

Although model order reduction methods for structures experiencing large-amplitude vibrations with geometric nonlinearities have been investigated for a long time [1, 2, 3, 4, 5], they have been only recently applied to the analysis of Micro-Electro-Mechanical Systems (MEMS), a class of devices with profound and increasing impact in the consumer and automotive market [6, 7, 8]. MEMS structures are generally actuated near resonance and are subjected to relatively large transformations. These effects are strongly enhanced by the fact that MEMS are monolithic devices often packaged in near-vacuum, thus limiting dissipation to negligible levels. As a consequence, they show highly nonlinear dynamical features that are rarely observed at the macro scale, ranging from jump phenomena [9], to bifurcations of solutions [10] (e.g. bistability [11]), internal resonances and saturation effects [12, 13, 14, 15], self-induced parametric amplification [16] and frequency combs [17, 18]. Furthermore, the nonlinear properties of MEMS can be tailored to yield performance that would not be accessible operating in the linear regime [19]. Accurate and predictive modeling needs to account for all these aspects.

However, relying on Full Order Models (FOMs) for the numerical simulation of the structural behavior of MEMS, e.g., finite element models, poses severe computational challenges that have been only partially solved so far. Generally, one is interested primarily in the steady-state periodic response of MEMS as a function of the actuation intensity and frequency, i.e., the so-called Frequency Response Function (FRF) of selected output quantities of interest like, e.g., the maximum midspan deflection of a beam, or the rotation amplitude of a micromirror. Moreover, the actuation can be electrostatic, piezoelectric, or magnetic, according to the considered applications, hence introducing additional sources of nonlinearity. Finally, because of the large quality factors involved, ultimately leading to long transients, time marching schemes are hardly computationally affordable. Recent advancements on the topic have enabled FOMs simulations within reasonable computational times [20, 21]. Geometrical and inertial nonlinearities can be modeled using Harmonic Balance (HB) approaches or shooting techniques, which directly compute the periodic response. However, these approaches entail huge computational costs when applied to large Finite Element Method (FEM) models of MEMS. This motivates the interest in developing rapid and reliable Reduced Order Models (ROMs) that ensure a fast and accurate estimation of the FRF of structures within time spans that are compatible with industrial design requirements.

*giorgio.gobat,andrea.opreni,attilio.frangi@polimi.it
†stefania.fresca,andrea.manzoni@polimi.it

A large family of ROMs, which we can refer to as *linear* ROMs, gathers Galerkin projections onto low-dimensional linear subspaces. One of the simplest options is to use a selection of linear eigenmodes and resort to procedures like the STiffness Evaluation Procedure (STEP), first introduced in [22] to compute coupling coefficients. However, as recently highlighted in [23, 24], its application to 3D FEM models is critical since it is mandatory to explicitly include all the coupled high frequency (e.g. axial, lateral contraction) linear modes which are usually difficult to identify and costly to compute. This issue has been overcome by the Implicit Condensation (IC) approach, which has been successfully applied to MEMS only recently [6, 7, 25, 26]. In this case, a small subset of linear eigenmodes, known as master modes, is defined to span a stress manifold that statically condenses all the contributions of high frequency modes. However, when inertia nonlinearities play a major role or the frequencies of the slave modes are not well separated from the master ones, the method fails [27, 28, 29]. Another linear ROM relies on *Proper Orthogonal Decomposition* (POD) [2, 30, 31, 32, 33], which this contribution focuses on. In this case, basis functions are computed in a data-driven manner, performing the singular value decomposition of a matrix of FOM solutions computed over time, and for suitably sampled parameter values; thanks to SVD, the most relevant contributions to explain the solution variability across the time span and the parameter space are selected, resorting to an energy measure. Later, a Galerkin projection onto the POD subspace allows us to generate a low-dimensional ROM, which we refer to as POD-Galerkin ROM. In this contribution, we show how this approach can overcome the limitations shown by other linear methods.

An alternative to linear ROMs is provided by a different class of methods, which we can refer to as *nonlinear ROMs*. Among them, a further classification can be proposed with respect to the assumptions used in their derivation. Modal Derivatives and the related Quadratic Manifold approach [34, 35, 36, 37] try to define spaces of nonlinear basis functions with the key idea of taking into account the amplitude dependence of mode shapes and eigenfrequencies. However, these functions are assumed to be velocity independent, ultimately introducing model limitations similar to the IC approach [27, 38].

On the other hand, truly nonlinear reduction methods start by defining a nonlinear relationship between the original coordinates and those of the reduced dynamics, hence providing a more accurate treatment of the nonlinear trajectories and faster convergence with fewer master modes. This class of methods resorts to the concept of Nonlinear Normal Mode (NNM), whose study began with the pioneering work by Rosenberg [39]. In his work, the NNM was defined as a synchronous vibration of the system. This concept has been later generalized by the notion of invariant manifold [40, 41, 42, 43] and spectral submanifold [44, 45]. While the numerical computation of NNMs for large-scale FEM models has been tackled, e.g., in [46], the generation of ROMs based on the concept of NNM has been addressed so far for small systems with few degrees of freedom (dofs) and only in very recent contributions [47, 48] the technique has been applied to complex structures involving inertia and geometrical nonlinearities. However, its extension to multiphysics (e.g. electromechanics) has not been addressed yet, and poses severe computational challenges.

Early applications of POD [49, 2, 50] to elastic structures with distributed nonlinearities have put in evidence its optimality in the sense that it minimizes the average distance between the original signal and its reduced linear representation. Indeed, the linear nature of a POD-Galerkin approach can be considered as an advantage since few manipulations are needed to construct the ROM. Nevertheless, it also represents a drawback, because a single, global linear subspace might not be able in principle to describe the nonlinear invariant manifolds [51] which characterize mechanical structures. While applications of POD to MEMS [52, 53] have been so far mainly limited to linear mechanics, beam theory and optimization problems, in this contribution we focus on the application of POD to highly nonlinear problems, showing its accuracy and computational efficiency. In particular, different sources of nonlinearities are considered, dealing with large rotations, internal resonances (i.e. nonlinear coupling) and electrostatic forcing. The POD-Galerkin ROM is validated against FOM solutions, and its generalization capabilities over the space of parameters are assessed. In particular, the ROM dynamics is solved by resorting to numerical continuation and bifurcation analysis tools, which give an insight onto the underlying dynamics – being this latter usually difficult to access in the FOM case because of the high computational cost required. The POD-Galerkin ROM solution is also studied from the perspective of invariant manifold theory. In particular, we compare the periodic orbits obtained from the POD-Galerkin ROM and the invariant manifold approximated with the Direct Normal Form (DNF) approach [48] applied to the corresponding FEM system, providing a detailed analysis unprecedented for large Finite Element Models.

The structure of the paper is as follows. After a short description of the POD-Galerkin framework in Section 2, we focus on a series of applications to MEMS modeled with the FEM, ranging from simple beam resonators to complex micromirrors and to arches displaying internal resonances, which put a strain on known techniques for geometrical nonlinearities. In the examples, we discuss the physical rationale behind the POD modeling capabilities, resorting to comparisons with the results from the Direct Normal Form approach. We finally show that the POD-Galerkin ROM yields great promise also on coupled multiphysics applications where few or no alternatives are available.

2 Formulation

Let us consider the framework of structures subjected to large transformations and small strains. This is the operating range of most microsystems since they are often actuated at resonance and large aspect ratios allow reaching large displacements within the linear elastic range of the material. In this framework, the Saint Venant-Kirchhoff constitutive model [54] is the most appropriate choice, and is given by

$$\mathbf{S} = \mathcal{A} : \mathbf{E}, \qquad \mathbf{E} = \frac{1}{2}\left(\nabla\mathbf{d} + \nabla^T\mathbf{d} + \nabla^T\mathbf{d}\cdot\nabla\mathbf{d}\right); \tag{1}$$

where $\mathbf{S}$ is the second Piola-Kirchhoff strain tensor, $\mathcal{A}$ the fourth-order elasticity tensor and $\mathbf{E}$ the Green-Lagrangian Strain tensor. Here we denote by $\mathbf{d}$ the displacement field and by $\nabla(\cdot)$ the (material) gradient defined with respect to the reference configuration. The weak form of the linear momentum conservation law is:

$$\begin{aligned}\int_{\Omega_0} \rho_0 \ddot{\mathbf{d}}\cdot\mathbf{w}\,\mathrm{d}\Omega_0 + \int_{\Omega_0} \mathbf{P}[\mathbf{d}] : \nabla^T\mathbf{w}\,\mathrm{d}\Omega_0 = \\ \int_{\Omega_0} \rho_0\mathbf{F}\cdot\mathbf{w}\,\mathrm{d}\Omega_0 + \int_{S_T}\mathbf{f}\cdot\mathbf{w}\,\mathrm{d}S_0, \quad \forall\mathbf{w}\in H_0^1(\Omega_0),\end{aligned} \tag{2}$$

where the integrals are expressed in the reference configuration Ω_0 and $\dot{\square}$ denotes the time derivative. Here ρ_0 denotes the initial density, $\mathbf{P}[\mathbf{d}] = (\mathbf{1} + \nabla\mathbf{d})\cdot\mathbf{S}$ the first Piola-Kirchhoff stress tensor, $\mathbf{F}$ the body forces per unit mass, $\mathbf{f}$ the surface tractions prescribed on the surface S_T and $\mathbf{w}$ the test velocity selected in $H_0^1(\Omega_0)$, i.e. the space of functions with finite energy that vanish on the portion $S_U \subset \partial\Omega_0$ where Dirichlet boundary conditions are prescribed. In our applications we assume that vanishing displacements are enforced on S_U. Within the present context, it is worth stressing that Eq. (2) exactly accounts for geometric (elastic and inertia) nonlinearities, e.g., large rotations or nonlinear mode coupling.

The spatial discretization of Eq. (2), e.g. by means of finite elements, also including a Rayleigh model damping term, yields a system of coupled nonlinear differential equations of the following form:

$$\mathbf{M}\ddot{\mathbf{D}} + \mathbf{C}\dot{\mathbf{D}} + \mathbf{K}\mathbf{D} + \mathbf{G}(\mathbf{D},\mathbf{D}) + \mathbf{H}(\mathbf{D},\mathbf{D},\mathbf{D}) = \mathbf{F}(\mathbf{D},\boldsymbol{\beta},\omega,t), \qquad t\in(0,T) \tag{3}$$

where the vector $\mathbf{D}\in\mathbb{R}^n$ collects all unknown displacement nodal values, $\mathbf{M}\in\mathbb{R}^{n\times n}$ is the mass matrix, $\mathbf{C} = \omega_0/Q\mathbf{M}$ the Rayleigh model mass proportional damping matrix – considering a reference eigenfrequency ω_0 and a quality factor Q – and $\mathbf{F}\in\mathbb{R}^n$ the nodal force vector which depends on the actuation intensity parameters $\boldsymbol{\beta}$, the angular frequency of the actuation ω and in general also on $\mathbf{D}$, e.g. in electromechanical applications. The internal force vector has been exactly decomposed in linear, quadratic, and cubic power terms of the displacement: $\mathbf{K}\in\mathbb{R}^{n\times n}$ is the stiffness matrix related to the linearized system, while $\mathbf{G}\in\mathbb{R}^n$ and $\mathbf{H}\in\mathbb{R}^n$ are vectors given by monomials of second and third order, respectively. We stress that the components of these vectors can be expressed using an indicial notation

$$G_i = \sum_{j,k=1}^{n} G_{ijk}D_jD_k, \quad H_i = \sum_{j,k,l=1}^{n} H_{ijkl}D_jD_kD_l, \qquad i = 1,\ldots,n.$$

Eq. (3) represents our high-fidelity FOM which depends on the input parameters $\omega, \boldsymbol{\beta}$. The FOM can be solved in different ways and in the present work we consider two alternatives: a time marching scheme, i.e. a nonlinear Newmark algorithm, and an HB solver as developed in [21]. It should be recalled that in resonating MEMS an important output of interest is the FRF in which a selected quantity, like the midspan deflection of a beam or the rotation of a micromirror, is plotted versus ω for different $\boldsymbol{\beta}$. Indeed, the focus is on frequency stability for the following main reason: resonators operate close to a reference frequency where the behavior should be predictable. For instance, in micromirrors the stability of the motion is required to guarantee the performance during the line scanning process and predicting correctly the hardening and softening behavior is of paramount importance. As a consequence we are interested in the steady state response of the device. This is the direct output of HB approaches which express the solution as the sum of Fourier series. However, HB solvers are not standard in commercial codes and might not be easily accessible. Moreover, their cost rapidly increases with the size of the Fourier basis thus requiring dedicated computing facilities. On the contrary, time marching schemes are always available, but transients before reaching the steady state condition are often prohibitively long due to the large quality factors of MEMS. As a consequence the choice of the solver is in general a trade-off which strongly depends on the application at hand. Several examples are commented in Section 3 where details on the simulation settings are provided.

2.1 Reduced order modeling through POD

The first step in the construction of a POD-Galerkin ROM requires to generate a matrix $\mathbf{X} \in \mathbb{R}^{n\times m}$, whose m columns collect snapshots of the FOM solutions, obtained for different values of the parameters $\omega, \boldsymbol{\beta}$. If the FOM is solved by means of an HB approach, the snapshots for a given frequency are taken at regular intervals over one single period of the steady state response by reconstructing the displacement field starting from the Fourier coefficients. Otherwise, if time marching schemes are employed, several alternatives are indeed available according to whether snapshots are taken in a condition close to the steady state or not. The influence of these choices is extensively investigated in Section 3.

Next, the Singular Value Decomposition (SVD) of the matrix $\mathbf{X}$ is computed,

$$\mathbf{X} = \mathbf{U}\boldsymbol{\Sigma}\mathbf{V}^T$$

where the columns of the orthonormal matrix $\mathbf{U} \in \mathbb{R}^{m\times m}$ are the left singular vectors, often called Proper Orthogonal Modes (POMs) in the literature [2, 30, 31]; the columns of the orthonormal matrix $\mathbf{V} \in \mathbb{R}^{n\times n}$ are the right singular vectors. The diagonal elements of $\boldsymbol{\Sigma} \in \mathbb{R}^{m\times n}$ are the singular values of the matrix $\mathbf{X}$ and are conventionally ordered from the largest to the smallest. In particular, the rank of $\mathbf{X}$ is equal to the number of nonzero singular values, and the optimal rank-p approximation $\tilde{\mathbf{X}}$ of $\mathbf{X}$, in a least squares sense, is given by the rank-p SVD truncation

$$\tilde{\mathbf{X}} = \sum_{i=1}^{p} \sigma_i \mathbf{U}_i \mathbf{V}_i^T$$

in which σ_i is the i-th singular value contained in the diagonal of $\boldsymbol{\Sigma}$, $\mathbf{U}_i$ is the i-th column of $\mathbf{U}$ and $\mathbf{V}_i$ is the i-th column of $\mathbf{V}$. See, e.g., [30] for further details. The SVD of $\mathbf{X}$ provides important insight into the energy distribution of the snapshots where the energy of $\mathbf{X}$ is defined via the Frobenius norm:

$$\varepsilon(\mathbf{X}) = \|\mathbf{X}\|_F^2 = \sum_{i=1}^{n}\sum_{j=1}^{m} x_{ij}^2 = \sum_{k=1}^{\min(m,n)} \sigma_k^2.$$

The POD approach selects the first p most energetic POMs to build the POD-Galerkin ROM approximation:

$$\mathbf{D} \approx \sum_{i=1}^{p} Q_i \mathbf{U}_i \tag{4}$$

where Q_i are the ROM generalized coordinates. Hence, the POD-Galerkin approximation of $\mathbf{D}$ in (4) is given by a linear combination of POD modes, and the resulting trial subspace is optimal in the sense that it captures the highest possible energy content among all possible linear subspaces for any prescribed dimension p. Furthermore, the error in the snapshots approximation is related to the sum of the square of the singular values associated to the nonretained modes [30].

Once the linear trial POD subspace has been obtained, projecting the FOM (3) onto the POD subspace yields the structural dynamics geometric POD-Galerkin ROM, under the form of a p-dimensional nonlinear ODE system, whose solution provides the dynamics of the generalized coordinates:

$$\begin{aligned}\mathbf{M}^{\mathrm{POD}}\ddot{\mathbf{Q}} + \mathbf{C}^{\mathrm{POD}}\dot{\mathbf{Q}} + \mathbf{K}^{\mathrm{POD}}\mathbf{Q} + \mathbf{G}^{\mathrm{POD}}(\mathbf{Q},\mathbf{Q}) \\ + \mathbf{H}^{\mathrm{POD}}(\mathbf{Q},\mathbf{Q},\mathbf{Q}) = \mathbf{F}^{\mathrm{POD}}(\mathbf{Q},\boldsymbol{\beta},\omega,t), \quad t\in(0,T)\end{aligned} \tag{5}$$

where

$$\mathbf{M}^{\mathrm{POD}} = \mathbf{U}^T\mathbf{M}\mathbf{U}, \quad \mathbf{C}^{\mathrm{POD}} = \mathbf{U}^T\mathbf{C}\mathbf{U}, \quad \mathbf{K}^{\mathrm{POD}} = \mathbf{U}^T\mathbf{K}\mathbf{U},$$
$$\mathbf{F}^{\mathrm{POD}} = \mathbf{U}^T\mathbf{F}, \quad G_i^{\mathrm{POD}} = g_{ijk}^{\mathrm{POD}} Q_j Q_k, \quad H_i^{\mathrm{POD}} = h_{ijkl}^{\mathrm{POD}} Q_j Q_k Q_l,$$

with $\mathbf{M}^{\mathrm{POD}}, \mathbf{C}^{\mathrm{POD}}, \mathbf{K}^{\mathrm{POD}} \in \mathbb{R}^{p\times p}$. The computation of the vectors $\mathbf{G}^{\mathrm{POD}}$ and $\mathbf{H}^{\mathrm{POD}}$ entails $O(p^3)$ and $O(p^4)$ terms, respectively. Note that the coefficients g_{ijk}^{POD} and h_{ijkl}^{POD} can be precomputed, and that the reduced problem can be assembled efficiently thanks to its polynomial nature, thus avoiding the use of hyper-reduction techniques such as the (discrete) empirical interpolation method [55, 56, 57].

2.2 Solution of the Reduced Order Model

One of the greatest benefits of generating a POD-Galerkin ROM as the one in Eq. (5) is the possibility to compute directly periodic solutions and trace the full FRF, with both stable and unstable branches, by resorting to continuation codes either based on HB techniques or collocation approaches. Some well-known packages, suitable for small scale problems, are available in the literature. One of the most relevant examples is `Auto07p` [58], a package that uses collocation methods in `FORTRAN` to perform numerical continuation and bifurcation

analysis. Among other tools we can mention `Manlab`, a `Matlab` package that uses HB method and Asymptotic Numerical Method [59, 60]; `Nlvib` that also exploits HB methods [61]; `COCO` that implements collocation methods and algorithms for bifurcation detection [62]. Another excellent package able to perform the continuation of ODEs is `BifurcationKit` [63], an emerging toolkit for Julia language that provides continuation methods for ODEs and PDEs. These packages usually provide the ability to distinguish between stable and unstable branches, locate bifurcation points and follow alternative branches of the solution. We highlight that the same versatility is difficult to achieve with a FOM. Indeed, even if a HB formulation with continuation has been recently proposed in [20, 21] for large scale problems, computing times are not compatible with their application at the design or prototyping levels.

In this work, we compute solutions with `Manlab`, which has an impressive capability to perform accurate bifurcation analysis and to exploit the Asymptotic Numerical Method [64] by ensuring a good balance between computational time and accuracy, provided that the problem can be re-written in quadratic form.

2.3 POMs and reconstruction vectors provided by the Direct Normal Form approach

An important feature of an effective ROM is the capability to identify an invariant subspace for the system dynamics, i.e. trajectories initiated along the subspace remain within the subspace itself in the full order solution. In linear systems each mode defines an invariant plane in the phase space, hence linear projection methods as the modal decomposition provide an excellent tool for generating ROMs. On the other hand, in presence of geometric nonlinearities, invariance of modal subspaces is not guaranteed as underlined in past works, for instance by Amabili and Touzé [51] and Haller [65]. Indeed, the invariant manifold tangent at the origin to a given modal subspace is a curved hypersurface that requires nonlinear methods. In this framework, the parametrization method for invariant manifolds initially formulated by Cabré, Fontich and de la Llave [66] and further studied by Haro [67, 68, 69] was recently applied to large scale finite element systems of mechanical structures [47, 48, 70] thanks to the Direct Normal Form approach. The fundamental idea of this class of methods is to parametrize the dynamics of the system along the invariant manifold associated to a subset of of its eigenfunctions, i.e. master modes. This requires the introduction of a nonlinear change of coordinates between the nodal displacements and the parametrization coordinates. Using the formulation proposed in [47], the nonlinear coordinates change for a single master-mode reduction in an undamped mechanical system is expressed as:

$$\mathbf{D} = \boldsymbol{\phi}_m R + \hat{\mathbf{a}} R^2 + \hat{\mathbf{b}} S^2 + \hat{\mathbf{c}} R^3 + \hat{\mathbf{u}} R S^2 + O(|R, S|^4), \tag{6}$$

where $\boldsymbol{\phi}_m$ denotes the eigenmode associated to the master mode. Here $\hat{\mathbf{a}}$, $\hat{\mathbf{b}}$, $\hat{\mathbf{c}}$, and $\hat{\mathbf{u}}$ are higher order reconstruction vectors used to map the parametrization coordinates R and S to the physical displacement $\mathbf{D}$. The expression in Eq. (6) considers up to third-order contributions, nevertheless it can be expanded up to the desired order following the procedure presented in [71]. The reconstruction vectors in Eq .(6) apply a correction with respect to a simple modal decomposition approach by accounting for the coupling between master and slave modes. As shown by Shaw and Pierre [72] and more recently by Buza [65], the projection of the eigenfunctions of the system along quadratic reconstruction vectors provides a solid framework to identify the modes that better embed the curvature of the invariant manifold. This last result is the natural extension of what remarked by Amabili and Touzé [51] where the trial space identified by POD was interpreted as the best linear approximation of the nonlinear normal mode. The consequence is that, in order to properly build a ROM relying on methods such as POD, one needs to introduce also bases that allow a correct approximation of the manifold curvature. This is highlighted in the results section, where qualitative changes in the predicted structural response are obtained by adding POMs with apparent negligible energy contribution, however showing a high curvature related to the invariant manifold of the system. This effect can also be observed in their shape, which resembles that of the reconstruction vectors provided by the DNF. An important remark is that in the upcoming comparisons the DNF reconstruction vectors are derived by imposing their orthogonality with respect to the linear master subspace. This choice makes the method equivalent to a graph style parametrization of the system.

3 Purely mechanical applications

Four mechanical benchmark cases are here proposed to discuss the accuracy of POD-Galerkin ROMs: a doubly clamped beam, two micromirrors and a shallow arch. In all cases, FEM meshes are made of wedge quadratic elements ("extruded" isoparametric elements with 15 nodes). For each example we report in A the computation time required by the FOM, the offline and the online stages of the ROM.

3.1 Doubly clamped beam

Let us consider a doubly clamped beam of length $L = 1000\,\mu$m with a rectangular cross-section of dimensions $10\,\mu\text{m} \times 24\,\mu\text{m}$, as depicted in Fig.1.

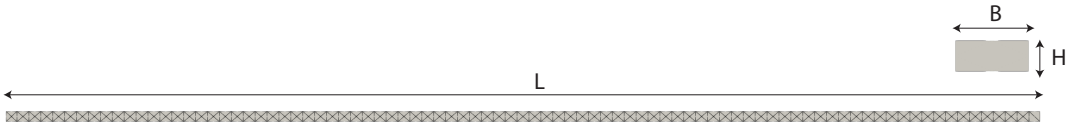

Figure 1: Geometry and mesh of the doubly clamped beam, front view and cross-section

This academic example simulates realistic MEMS resonators like those analysed in [7]. A rather coarse mesh with 2607 nodes has been employed. Indeed, this example is used to discuss extensively the features of the ROM and every result is compared with reference FOM solutions that are affordable only with relatively coarse meshes. The beam is made of isotropic polysilicon [73], with density $\rho = 2330\,\text{Kg/m}^3$, Young modulus $E = 167\,\text{GPa}$ and Poisson coefficient $\nu = 0.22$. We select a fixed quality factor $Q = 50$. The device vibrates according to its first bending mode at $f_0 = 87141\,\text{Hz}$. The first five eigenfrequencies are reported in Table 1.

Eigenmode	1	2	3	4	5
Frequency [kHz]	87.141	208.45	240.03	470.10	572.18

Table 1: Doubly clamped beam: eigenfrequencies

The external excitation is provided by a body load proportional to the first eigenmode $\mathbf{F} = \mathbf{M}\boldsymbol{\phi}_1 \beta \cos(\omega t)$ with β load multiplier. The training data can be generated with different methods and a variable number of snapshots. Since we aim at modeling the steady-state response of the system, HB solutions are the ideal candidates to generate representative data. In a first application, we consider a training dataset computed with HB and $\beta = 0.5\,\mu$N and consisting of a total of 2000 snapshots generated from 10 data points represented by the violet circle markers on the FRF in Figure 2a). Each data point corresponds to a periodic solution on which 200 snapshots are taken at regular intervals.

First, we address the convergence with respect to the number of POMs retained in the subspace. The POD method usually adopts the relative energy as a convergence measure to select the space dimension. The relative energy content of each POM is depicted in Figure 2b). It is worth stressing that the first POM represents 99.995 % of the energy and the second POM contains only the 0.0035 %. To test the convergence of the ROM, we consider seven different subspaces with 1,2,3,4,6,8 and 10 POMs, respectively. The resulting ROMs are tested on $\beta = 0.5\,\mu$N (i.e. the same forcing level applied during the training stage) and $\beta = 0.75\,\mu$N. The resulting FRFs are plotted in Figure 2c). We notice that trial spaces with less than 3 POMs are inadequate to describe the dynamics, while richer spaces provide a very good accuracy. It should be remarked also that increasing the number of POMs a mild 1:5 internal resonance is evidenced, as predicted by the FOM, see Figure 2d).

Next, keeping 6 POMs in the trial space, a choice that guarantees a good balance between efficiency and accuracy, the ROM is tested on the forcing levels $\beta = 0.25, 0.375, 0.45, 0.5, 0.625, 0.75, 1.0\,\mu$N. The results are reported in Figure 3 where they are compared to the solutions of the HB-FOM, when available. The two families of simulations are almost exactly superimposed, hence proving a good predictive capability of POD beyond the training range but still under akin dynamic behaviour. Also, the correct evolution of the unstable branch is reproduced, from mildly to strongly hardening at increasing actuation levels. Nevertheless, such capabilities are restrained to the class of solutions embedded in the trial subspace. Consequently, when major changes occur, like e.g. strong internal resonances, the ROM is expected to provide wrong predictions.

Nevertheless, the proposed solution exploits a large number of snapshots that may be not easily accessible on very large models. Consequently, we investigate the performance of the ROM when progressively and drastically decreasing the number of sampling instances while keeping six POMs in the basis. We consider six different sets of HB snapshots, each with a single data point on the FRFs corresponding to the β, ω values defined in the legend of Fig. 4a). Points are taken both close and far from the peak in order to test the potential influence of their specific location. Four sets contain a total of 150 snapshots each sampled along the selected periodic response; two sets finally consist of only 30 snapshots taken on the FRF with the lowest β and far from resonance. The predicted FRFs at $\beta = 0.75$ are depicted in Figure 4b)-d). The FRFs match the FOM and only minor differences can be appreciated mainly in the region of the internal resonance, hence suggesting an unexpected robustness of the method with respect to the number of snapshots used in the training stage. It appears that, whenever the actuation level and frequency are reasonably close to the actual operative parameters of the device, a very good match is recovered.

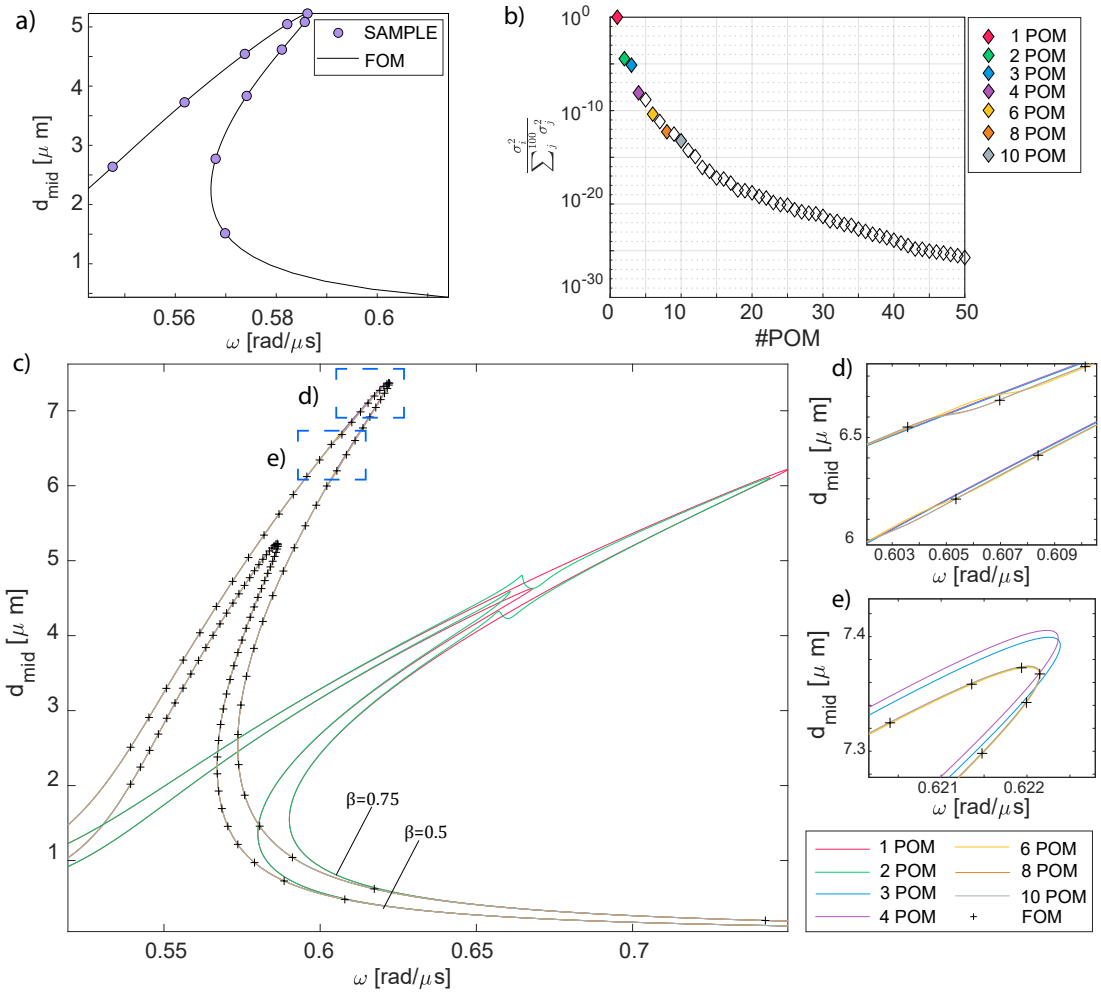

Figure 2: Doubly clamped beam: convergence with respect to the number of POMs retained in the ROM. Figure a): sampling points illustrated on the FOM FRF computed with the HB. Each point corresponds to a periodic solution along which snapshots are collected. Figure b): relative energy content of POMs. Figure c): FRF of the midspan displacement d_{mid} computed with each ROM subspace considered. Figures d) and e): enlarged views of the resonance peak and the internal resonance interaction region, respectively.

However, HB solvers might not be accessible in general (e.g. in commercial codes), or might simply be too costly. In these cases time-marching methods are the only option available to generate snapshots. To highlight the possible differences with HB-FOM solutions in this simple and small example, we start considering three datasets computed with time marching methods and $\beta = 0.5\,\mu$N close to the steady state (SS). This means that, for any frequency considered, a sufficiently large number of cycles is first simulated so as to reach an approximate steady state condition before taking snapshots and then moving to the following frequency. The three datasets consist respectively of: 1242 snapshots sampled at 2 different frequencies; 6210 snapshots sampled at 10 different frequencies (including the ones of set 2); 12420 snapshots sampled at 20 different frequencies (including the ones of set 3). Finally, two sets have been generated from a fully transient (TR) response, far from steady state, at one single frequency, consisting of 1000 and 25 snapshots, respectively. The sampling points and plots of the time marching datasets are illustrated in Figures 5a)-c). The corresponding FRFs are displayed in Figure 5d). We notice that all the solutions are almost exactly superposed and the localized 1:5 internal resonance is the only portion of the FRFs where minor differences can be appreciated (Figure 5e)-f)). In particular, the capability of the technique to predict steady state solutions starting from fully transient data is impressive and very promising for MEMS applications where large quality factors generally prevent time marching schemes from reaching steady state conditions within reasonable time frames.

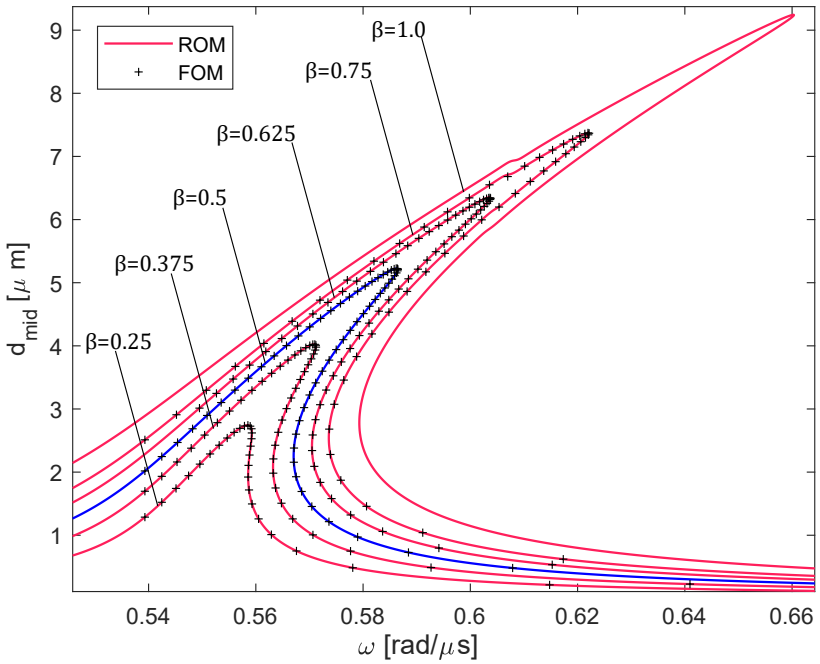

Figure 3: Doubly clamped beam: FRFs of the midspan displacement d_{mid} computed with the ROM with 6 POMs compared with the FOM solution. The blue line denotes the training curve, while the red ones are solutions computed for different levels of the forcing. The cross markers represent the FOM solutions

3.1.1 Comparison between POMs and DNF reconstruction vectors

As put in evidence in Figure 3, a major improvement comes from the inclusion of the third POM. The first three POMs are represented in Figure 6b). The difference between the trial spaces with 2 and 3 POMs is not easy to appreciate through a direct application of the energy criterion. From a physical perspective, the first two POMs closely resemble the first and the second symmetric bending modes, while the third POM is related to high frequency axial/contraction modes.

In linear methods based on modal subspaces, see e.g. [23, 24], it is now acknowledged that this type of modes must be imperatively included in the selected subspace to guarantee convergence, but they are difficult to identify a priori. These modes indeed provide an important correction to the kinematic field that cure the excessively hardening response of the reduced model obtained by projection on a linear subspace. The automatic identification of such a contribution can be considered as a major benefit of the POD over modal techniques.

Considering now the parametrization method of invariant manifolds discussed in Section 2.3, the reconstruction vectors of Eq. (6) are plotted in Figure 6a). We start noticing the striking analogy between the first eigenmode $\boldsymbol{\phi}_1$, the quadratic displacement-dependent term $\hat{\mathbf{a}}$, the cubic displacement-dependent term $\hat{\mathbf{c}}$ and the first three POMs. Next, in Figure 6 the manifold of the DNF is compared with orbits computed through POD by considering the phase space composed by the projection of the displacement and velocity on the first eigenmode and the projection of the displacement on the fourth eigenmode. The ROM solution lies almost perfectly on the approximated manifold, thus showing that the subspace computed with data-driven methods converges to the one computed with asymptotic expansions.

3.2 Micromirrors

Scanning micromirrors are witnessing explosive growth in recent years due to successful applications ranging from pico projectors for Augmented Reality (AR) lenses [74], to 3D scanners for Light Detection and Ranging (LiDAR) application. In this section we address two micromirrors with different nonlinear behavior. These devices are intrinsically nonlinear due to inertia effects associated with large rotations, and they present a frequency-amplitude dependence which might be either hardening or softening according to the specific layout. The correct quantitative prediction of nonlinear effects is a tough benchmark for any FOM or ROM. Recently, the authors have developed a large scale HB approach in [21] for the analysis of piezo mirrors which is here utilized as FOM to generate snapshots. It is worth stressing that classical ROM techniques like the Implicit Condensation [6] fails to provide the required accuracy.

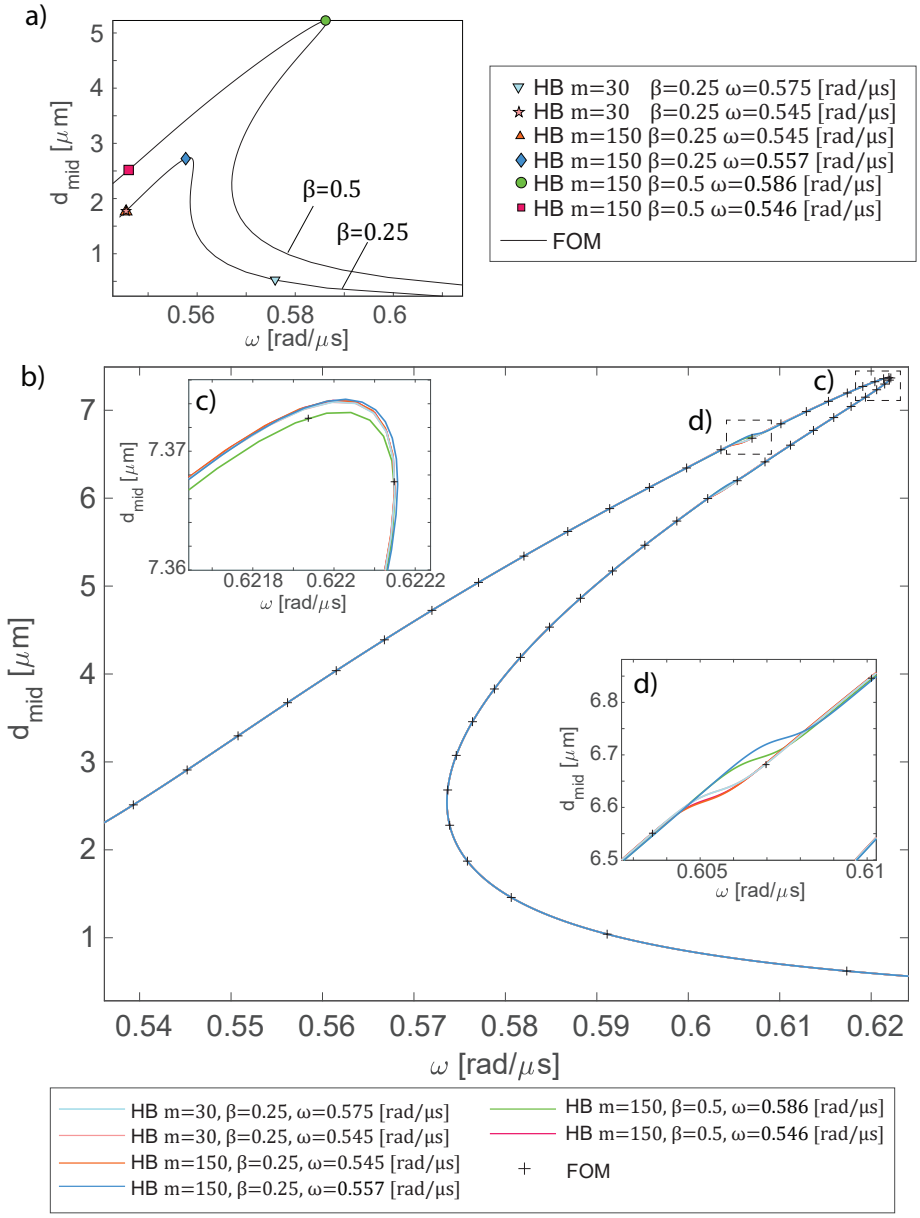

Figure 4: Doubly clamped beam: Figure a): sampling frequencies and forcing of the datasets HB considering a low number of snaphots. Each set contains samples referring to a single $\omega - \beta$ instance. Load level, frequency, method used and number of samples are reported in the legend. Figure b) presents the FRFs computed with the ROMs built on the set detailed in Fig.a) considering 6 POMs. Figure c) and d): close-up of the resonance peak and of the internal resonance region.

3.2.1 Micromirror 1

An optical image of the first micromirror, fabricated by STMicroelectronics [21, 75], is presented in Figure 7a). The top view is reported in Figure 7b). The reference FOM is built considering only half of the structure to exploit symmetry as illustrated in Figure 7c).

The central circular reflecting surface is directly attached to the substrate with two short torsional beams (springs), while the rotation of the mirror is induced by trapezoidal beams which are connected to the mirror through folded compliant springs. The beams are actuated by piezo-patches, i.e. PZT layers with a thickness of 2 μm appearing in Figure 7b) as light brown areas. The mirror disk has a diameter of 3000 μm and the lower surface has been reinforced with a curvilinear support in order to minimize the dynamic deformation of the mirror itself. The mirror is made of single crystal silicon with [110] orientation (see [76] for details) and the first five eigenfrequencies are reported in Table 2.

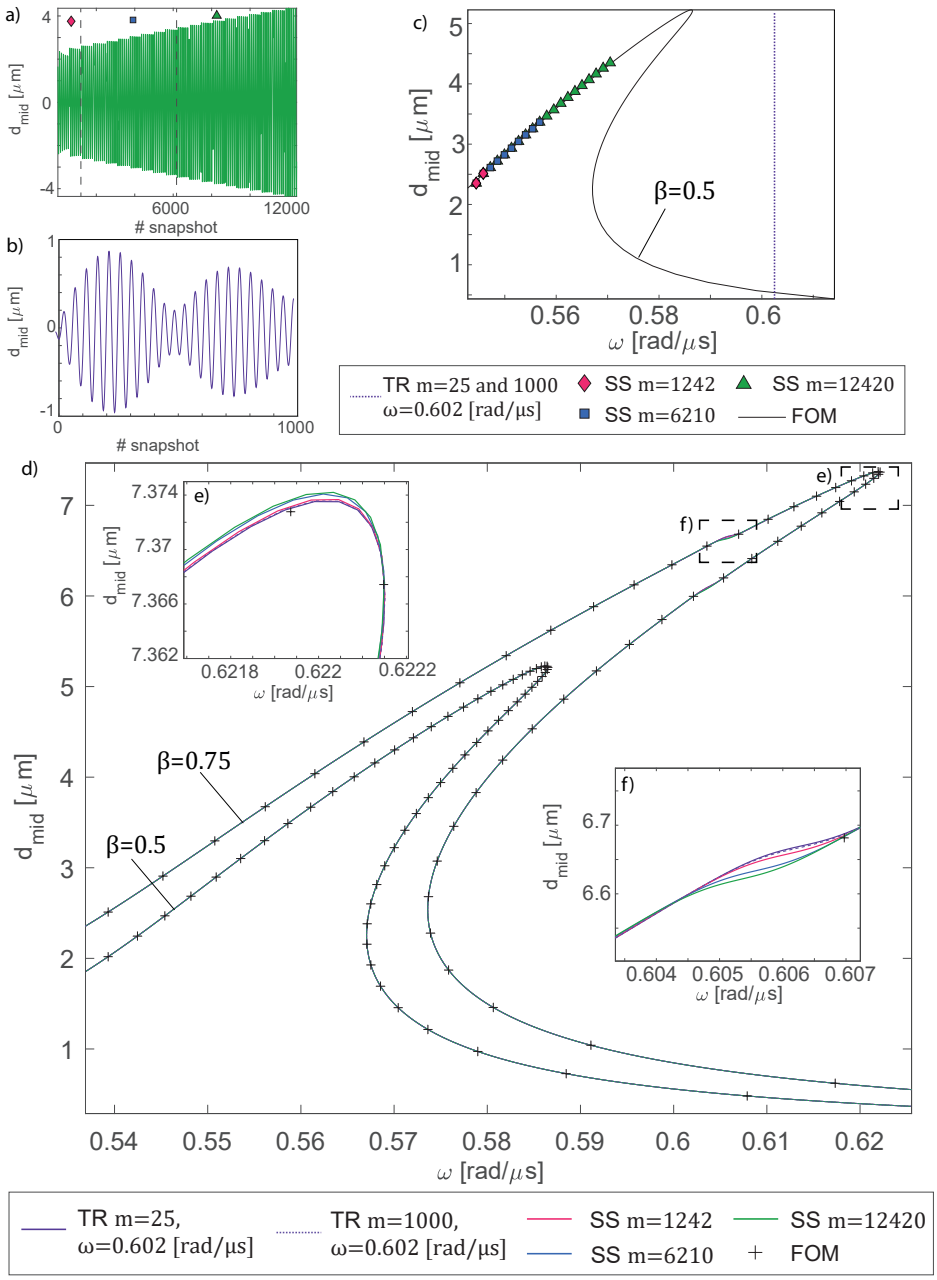

Figure 5: Doubly clamped beam. Comparison between different time marching training sets. Figure a): snapshot-sets taken during a time-marching analysis, close to Steady State (SS). The frequency is swept upwards and the data are collected after a fixed number of time steps. The time analyses are performed sequentially and jumps denote a change of the forcing frequency. Figure b): snapshot-sets collected during a fully transient (TR) time-analysis for a fixed frequency. Load level, method used and number of samples are reported in the legend. Figure c): sampling frequencies of the datasets SS and TR illustrated in the $\omega - \beta$ parameter space. The transient one is represented by the dotted vertical line. Figure d) presents the FRFs computed with the ROMs built on the set detailed in Fig.c) considering 6 POMs. Figure e) and f): close-up of the resonance peak and of the internal resonance region.

The quality factor is set to $Q = 100$. In our investigation, for the sake of simplicity, we replace the piezoelectric actuation with a body force proportional to the first eigenmode $\mathbf{F}(t) = \mathbf{M}\boldsymbol{\phi}_1 \beta \cos(\omega t)$ with β load multiplier. The FEM model in this benchmark contains a total of 15341 nodes.

In the training stage, in which the FOM has been solved with an HB approach, 5000 snapshots have been generated from frequency samples uniformly distributed over the FRF setting $\beta = 0.3\,\mu$N. Even if a POD-Galerkin ROM with 1 or 2 POMs collects more than 99.99% of the energy content (see Figure 8a), the trial space should contain at least the first 6 POMs to achieve convergence. Nevertheless the ROM with 6 POMs

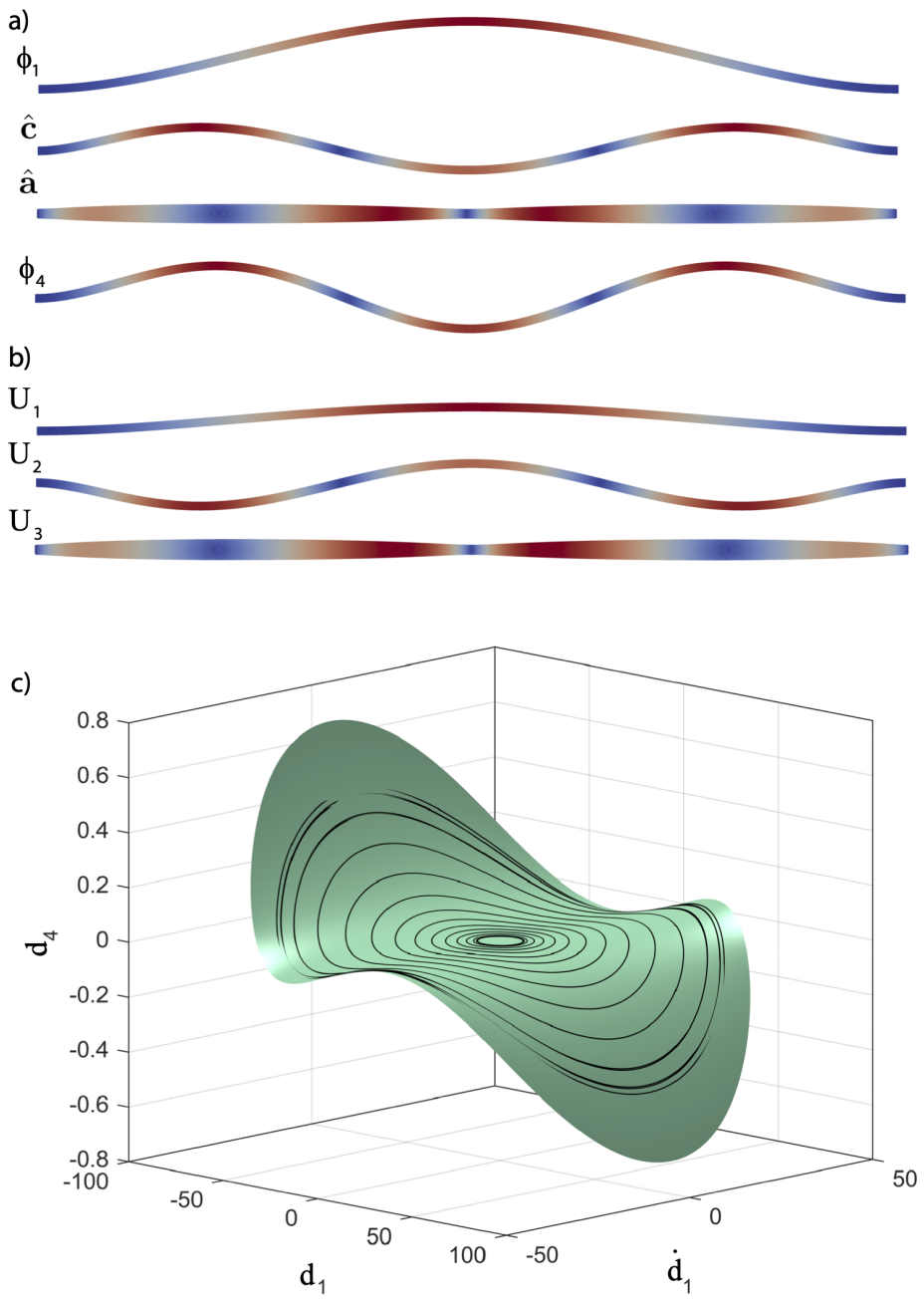

Figure 6: Doubly clamped beam. Comparison between the POD subspace bases and DNF. Figure a) shows the parametrization up to cubic order and the third eigenmode. Figure b): first three POMs. Figure c): invariant manifold computed with DNF (green surface) and orbits computed with POD (black lines). The manifold is defined in the phase space composed by the first eigenmode displacement and velocity and the fourth eigenmode displacement.

displays a small resonance effect close to $\omega = 0.0142$ that is eliminated by using 8 POMs. This can be appreciated from Figure 8b) where several FRFs have been computed with an increasing number of POMs.

For the subsequent analyses, a trial space with 8 POMs is retained. Different levels of the forcing have been tested as illustrated in Figure 9 showing that an excellent agreement is achieved together with a remarkable predictive capability. Only few curves are validated against the corresponding FOM solution because of the prohibitive computational cost entailed by the HB-FOM model. We also stress, for sake of completeness, that in this specific example the 8 POMs used guarantee a good accuracy and performance only up to $\beta = 0.3$, while for higher forcing levels some artefacts appear. These are still under investigation and are possibly associated with the very large operative rotations of the micromirror, that are difficult to model with a linear basis. We

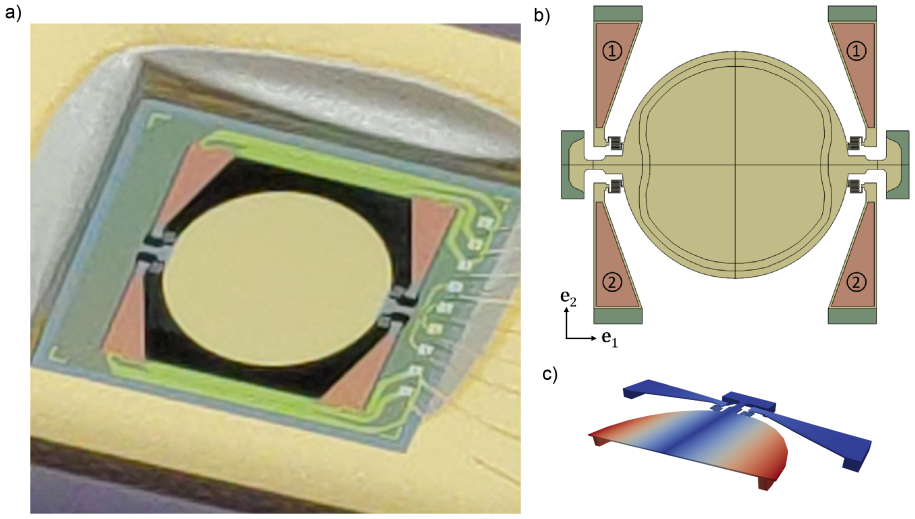

Figure 7: Micromirror 1. Figure a): photo of the real device. Figure b): top view of the layout. Piezoelectric patches are in light brown and the numbers characterize the actuation scheme [21, 75]. Figure c): first torsional mode. The eigenmode consists of a rotation of the micromirror plate as shown by the color-map of the displacement magnitude.

Eigenmode	1	2	3	4	5
Frequency [kHz]	2.258	7.238	23.378	23.426	56.046

Table 2: Micromirror 1: eigenfrequencies

remark however that is possible to recover a good approximation of the FRF for a load multiplier $\beta = 0.4$ if 24 POMs are included in the trial space (upper curve in Figure 9). Nevertheless, the increased dimension of the ROM drastically reduces the computational gain.

Similarly to the doubly clamped beam, some remarks concerning the POD subspace are worth stressing. The first 3 POMs are depicted in Figure 10. From a physical point of view, the first POM corresponds to the linear torsional eigenmode, while the second one corresponds to a contraction of the mirror plate that applies a correction to the linearized torsion. Indeed a linearized rotation, when extended to large angles, induces a non physical stretch of the structure. The higher order POMs correspond to the membrane and axial deformation of the deformable springs and beams.

Considering the parametrization of the DNF, in Figure 10a) we also plot the reconstruction vectors of Eq. (6). Apart from the obvious correspondence between the linearized mode and the first POM, we notice a strong correspondence between $\hat{\mathbf{a}}$ and the second POM and between $\hat{\mathbf{c}}$ and a combination of the third and the fourth POMs.

Finally, Figure 10c) presents the solution manifold in a phase space composed by the projection of the displacement and velocity on the first eigenmode and of the displacement on the second eigenmode. The manifold obtained with the DNF (continuous green surface) and the orbits obtained through the POD-Galerkin ROM are nearly superimposed as remarked also in the previous example. The strong connections between the POD and the DNF emerge hence as a distinctive feature of the POD approach.

3.2.2 Micromirror 2

The second mirror addressed, also fabricated by ST Microelectronics, is illustrated in Figure 11. In this case the mirror is suspended to a gimbal rather than being directly attached to the substrate with torsional springs. As a consequence, its nonlinear behavior turns softening.

The FOM uses a rather coarse mesh with 3244 nodes. The frequency of the torsional mode is 29271 Hz and the quality factor has been set to $Q = 1000$. The first 5 eigenfrequencies are listed in Table 3. Also in this application, we replace the piezoelectric actuation method with a body force proportional to the third eigenmode $\mathbf{F}(t) = \mathbf{M}\boldsymbol{\phi}_3 \beta \cos(\omega t)$ with β load multiplier.

This benchmark, which looks rather similar to the previous one, turns into a tough challenge for simulation approaches, mainly because the torsional mode is not the lowest-frequency one (it is the third) and is not well

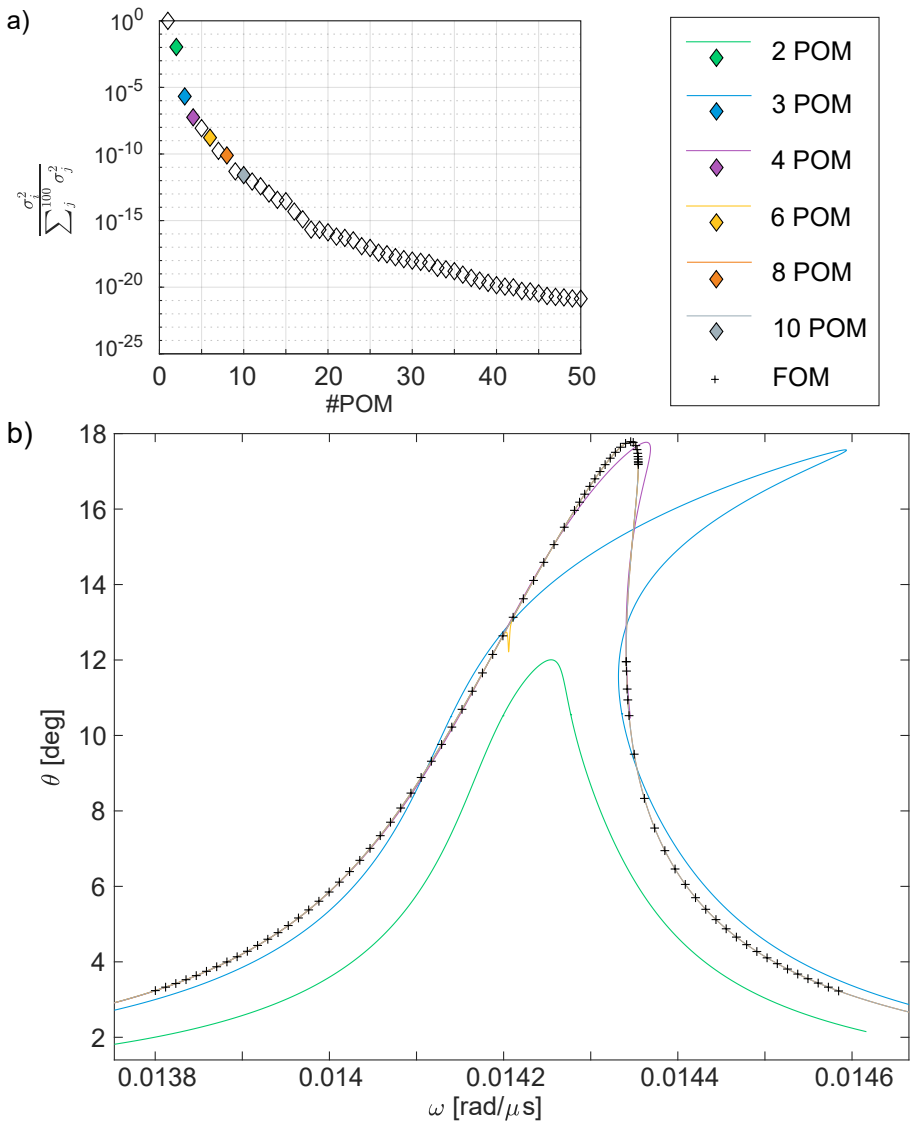

Figure 8: Micromirror 1: convergence of the ROM. Figure a): energy of each POM. Figure b): FRF for the ROMs including an increasing number of POM. The POD is tested on the training set. The ROM simulations progressively converge to the correct FOM solution. With 6 POMs a small resonance effect occurs close to $\omega = 0.0142[\text{rad}/\mu s]$ that is eliminated by further increasing the number of POMs

separated from the other modes. Indeed, in this case even the DNF requires a high order expansion and the quadratic formulation in [48] fails as detailed in [71]. The POD, on the contrary, performs indistinctly well. The training stage is performed considering $\beta = 2.5\,\mu$N and generating a total of 2000 snapshots. The distribution of the frequency samples on the FRF computed with the HB-FOM is presented in Figure 12a), while Figure 12b) collects the associated POMs. Testing different ROMs built with an increasing number of bases we obtain the results displayed in Figure 12c). The convergence of the subspace is consistent with the increasing number of POMs, and this can be appreciated from the enlarged views in Figures 12d) and 12e).

A good balance between subspace dimension and accuracy is given by the subspace spanned by 10 POMs on which we perform a more extensive testing stage varying, as usual, the force multiplier $\beta = 1, 1.5, 2, 2.5, 3\,\mu$N. The results plotted in Figure 13 show again the highly predictive capability of the POD-Galerkin ROM. Differently from the previous micromirror, the embedding subspace is able to provide good results also for forcing levels higher than the sampled one. This might be a consequence of the lower rotation amplitude in this case, always smaller than 15 degrees.

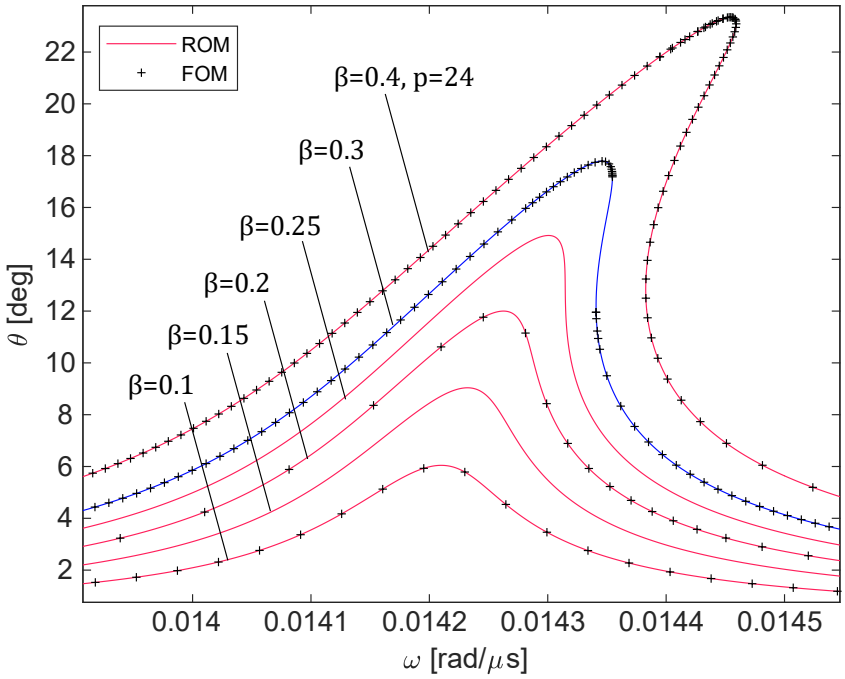

Figure 9: Micromirror 1: FRFs computed with the ROMs with 8 POMs compared with the FOM solution. The red continuous lines represent the ROM solutions computed in conditions different from the training data, the blue one marks the training condition curve. The cross markers represent the FOM solutions. The FRF with the highest β was obtained augmenting the number of POMs to 24.

Eigenmode	1	2	3	4	5
Frequency [kHz]	11.080	18.533	29.271	41.667	68.848

Table 3: Micromirror 2: eigenfrequencies

3.3 Shallow arch with internal resonance

In recent years several occurrences of complex nonlinear phenomena have been documented experimentally in MEMS, mainly due to their large quality factors Q. Internal resonances (IRs) play an important role in triggering more complex motions and facilitate energy transfer between modes. Often IRs are strongly linked to the stability of the associated periodic response and quasi-periodic regimes might arise as a consequence of Neimark-Sacker (NS) bifurcations [77]. The numerical prediction of such phenomena requires an accurate stability analysis which cannot be performed at a reasonable cost using FOMs, while can be much more conveniently run on small ROMs using dedicated continuation tools, as discussed in Section 2.2.

For these reasons we include among our benchmarks a shallow double-arch with a constant radius of curvature. The layout, inspired by the one proposed for a bistable structure in [78], has been suitably designed so as to trigger a 1:2 IR. The arch geometry and mesh are illustrated in Figure 14. The mesh considered consists of quadratic wedge elements and contains 1971 nodes.

The device is made of polycrystalline silicon with density $\rho = 2330\,\mathrm{kg/m^3}$ and a linear elastic Saint-Venant Kirchhoff constitutive model is assumed, with Young modulus $E = 167000\,\mathrm{MPa}$ and Poisson coefficient $\nu = 0.22$ [79]. The first six eigenfrequencies of the modelled structure are reported in Table 4.

Eigenmode	1	2	3	4	5	6
Frequency [kHz]	434.16	525.97	603.91	667.59	756.95	863.67

Table 4: First six eigenfrequencies of the MEMS arch

The quality factor has been set to $Q = 500$ and the actuation is provided by a body force proportional to the first eigenmode $\mathbf{F}(t) = \mathbf{M}\boldsymbol{\phi}_1 \beta \cos(\omega t)$ with β load multiplier.

In order to further stress the versatility of the POD-Galerkin ROM, we opt for time marching methods to simulate the FOM and generate the training dataset. Moreover, snapshots have been collected during the

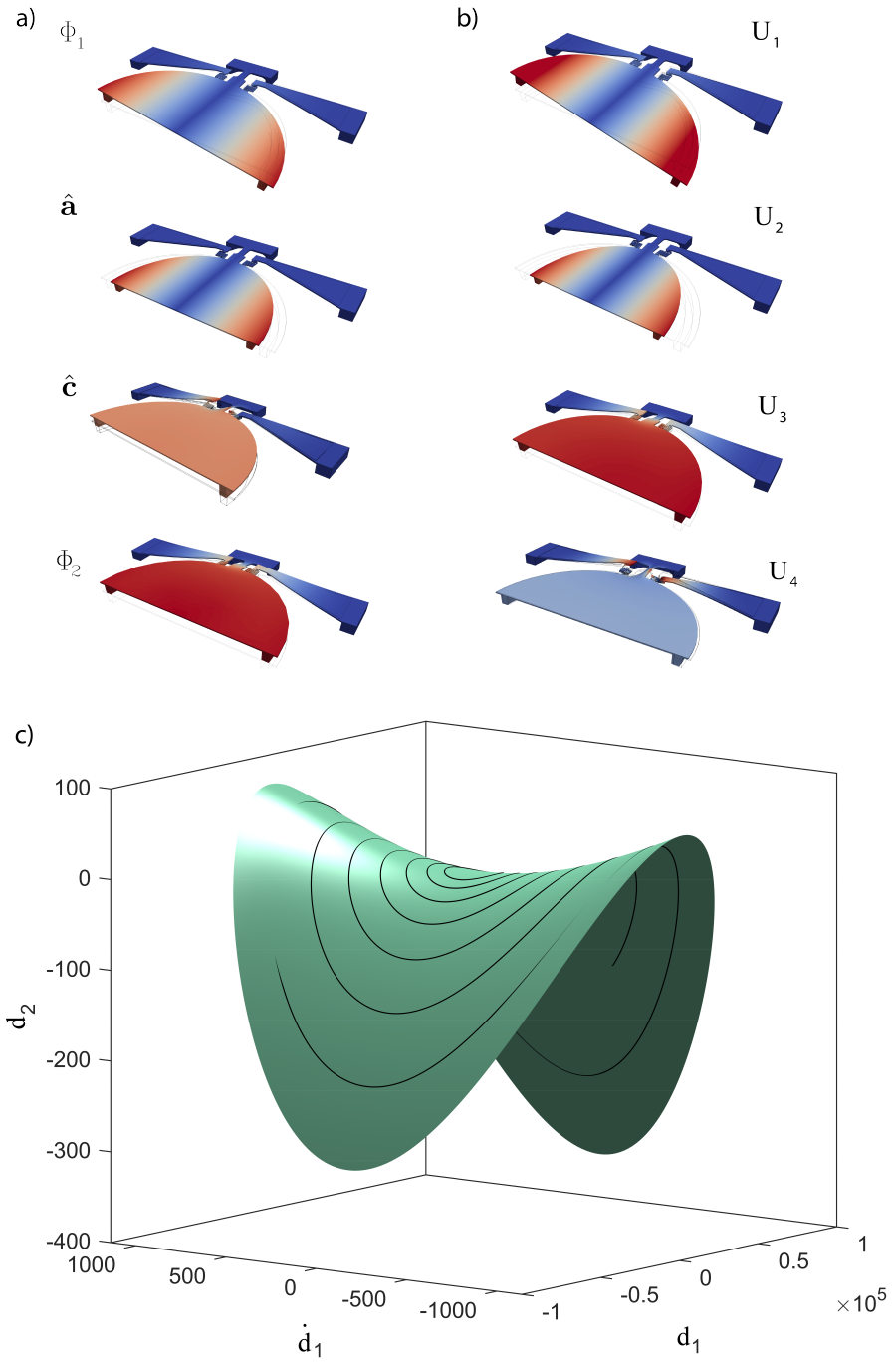

Figure 10: Micromirror 1: comparison between the POD subspace bases and DNF. Figure a): parametrization up to cubic order and the second eigenmode. Figure b): first three POMs. Figure 3): invariant manifold computed with DNF (green surface) and orbits computed with POD (black lines). The manifold is defined in the phase space composed by the first eigenmode displacement and velocity and the second eigenmode displacement

transient phase, far from steady-state conditions, according to the following strategy. The forcing level has been fixed to $\beta = 0.2\,\mu$N and a sequence of three frequencies have been analyzed with a Newmark implicit solver in a downward sweep. It is worth stressing that the three frequencies are selected almost randomly near the linear resonance of the device and are far both from the real peaks of the FRF and from the region of the quasi-periodic response, as commented hereafter. For each frequency, 100 cycles are simulated and a total of 30000 snapshots are collected. Initial conditions for the global analysis are homogeneous and the final state computed for each frequency yields the initial conditions for the next one. Given the Q value at hand, after 100 cycles the system is still fully in a transient phase. The frequency points and the time series of the mid-span deflection of the arch are collected in Figures 15a) and 15b), respectively.

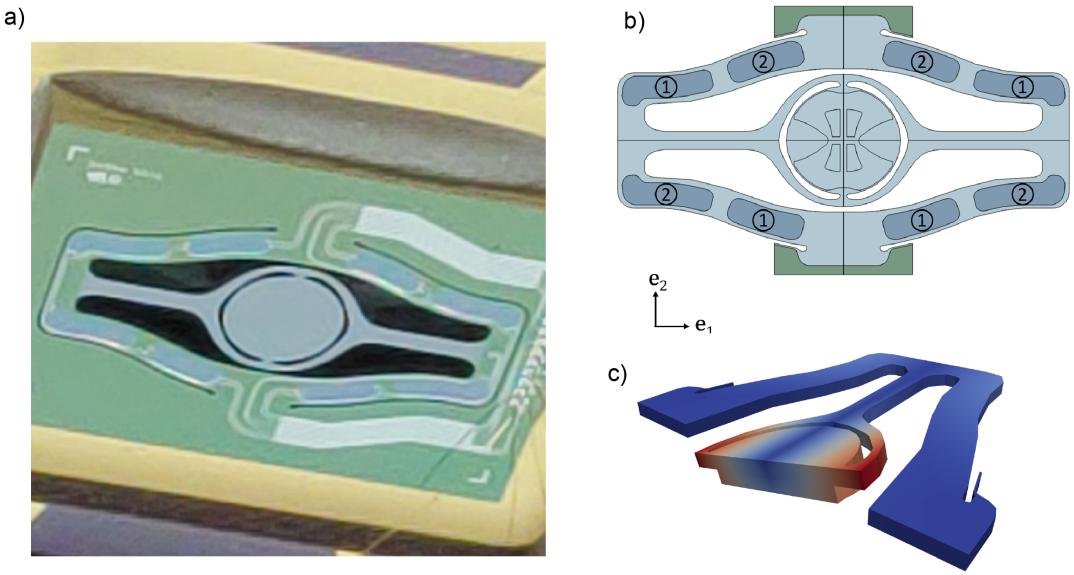

Figure 11: Micromirror 2. Figure a): optical picture of the micromirror. Figure b): top view of the layout. Piezoelectric patches are in light brown and the numbers characterize the actuation scheme [21, 75]. Figure c): third (torsional) eigenmode that is actuated during operations.

The SVD computed on the snapshot matrix yields the energy distribution of Figure 15c). Also in this case, although it appears that the energy is almost totally focused in the first two POMs, the convergence analysis presented in Figure 16a) shows that at least 4 POMs are required and a good convergence is achieved starting with 6 POMs. In the following, we will consider a trial space collecting the first 8 POMs. The dataset used in the training is quite large, but still affordable because of the small dimensions of the FEM model. Since the offline computation of the snapshots may be prohibitive in larger systems, the dependence on the number of snapshots and the reference parameters should be discussed. We explore such dependence by progressively down-sampling the snapshots collected. We use: 1) a dataset with half of the original data $m = 15000$, achieved by doubling the time step with respect to the original value, i.e. 50 points per period; 2) a dataset with $m = 7500$ i.e. 25 points per period; 3)-5) three dataset considering only one forcing frequency, $m = 2500$; 6) a dataset collecting only the last five cycles of the time history at frequency $\omega = 2.3\text{rad}/\mu\text{s}$, $m = 125$. The comparison between the datasets and 8 POMs reveals only negligible differences on the FRF and small variations in the bifurcation positions, see Figure 16c)-e). This portrait is expected since, as highlighted in the beam example, the dynamics can be easily captured only with few snapshots and the number of POMs is the dominant parameter.

The chosen ROM is now tested considering different forcing levels and the corresponding FRFs are plotted in Figure 17, together with the HB-FOM solutions. The model correctly reproduces the complex pattern of the 1:2 IR, as demonstrated by the shape of the frequency response displaying the two characteristic peaks. As recalled, a key feature of the ROM is the possibility to apply the bifurcation analysis tools discussed in Section 2.2 which yield the results of Figure 17. Two different classes of bifurcation points can be identified: saddle-node bifurcations, that split the FRF between unstable and stable branches, and Neimark-Sacker bifurcations that separate stable periodic and quasi-periodic regions. Quasi-periodicity is a dynamic condition where the external excitation frequency of the system is paired with an incommensurate smaller frequency that modulates the amplitude of the response (see [77] for further details). For a given FRF, in the region within the two Neimark-Sacker bifurcations only quasi-periodic, and eventually almost chaotic, solutions [77] are physically meaningful. This challenging benchmark shows that an excellent quality of the ROM can be achieved even with a fast training phase based on fully transient data.

4 Electromechanical coupled problems

While previous benchmarks have addressed purely mechanical problems with geometrical nonlinearities, the interest in generating an optimal linear trial space goes beyond these applications. In MEMS applications, multiple sources of additional nonlinearities come from the actuation mechanism and the most typical example is provided by electrostatic forces that depend in an intrinsically nonlinear manner on the displacement field.

In most contributions addressing both geometric and electrostatic effects (see e.g. [80, 81] for clamped-

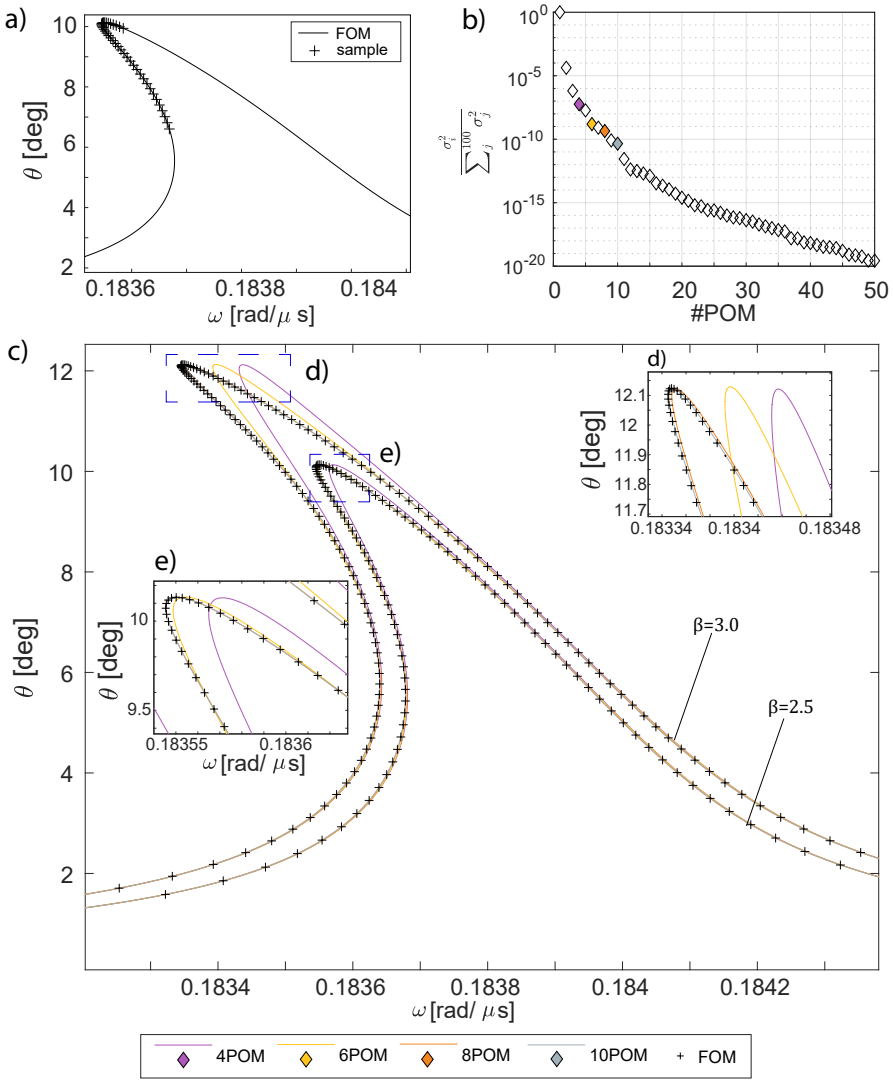

Figure 12: Micromirror 2: convergence of the ROM. Figure a): points of the FOM FRF utilized in the training phase to generate the snapshots. Figure b): energy content of each POM. Figure c): FRFs resulting from each ROM built with an increasing number of POMs. The POD is tested on the training set and on a second higher forcing level.

clamped beams) analytical approaches or simplified structural theories are utilized, although their application to real MEMS often leads to results that are only qualitatively correct or need careful device-dependent calibration. General numerical approaches are needed as MEMS might have complicated features that can be hardly reduced to simple models. However, a coupled electromechanical FOM able to simulate complex 3D structures is not a standard tool in most commercial codes and generating snapshots of the FOM solution often comes with a computational cost that may be unsuitable for practical applications.

Most importantly, a major difficulty of the POD is associated with the evaluation of the vector of nonlinear nodal electrostatic forces (EF). Popular data-driven algorithms like the Discrete Empirical Interpolation Method (DEIM) [82, 83] provide an optimal reconstruction of the full nonlinear vector starting from a collection of snapshots of the nonlinear forces. However, the DEIM is based on the assumption that few selected entries of the vector can be computed at a low cost independently of the others, while in electromechanical problems, the generation of the nonlinear vector of nodal forces has only a marginal cost with respect to the solution phase of the electrical sub-problem, be it solved with iterative integral equation approaches or with FE techniques. The development of a fast algorithm to circumvent this obstacle is still an open issue.

On the contrary, a simplified way to account for EFs through POD-based models can be done by exploiting the same approach successfully applied with the implicit condensation method in [7].

We assume that the trial space defined from snapshots given by the mechanical simulations is sufficiently rich

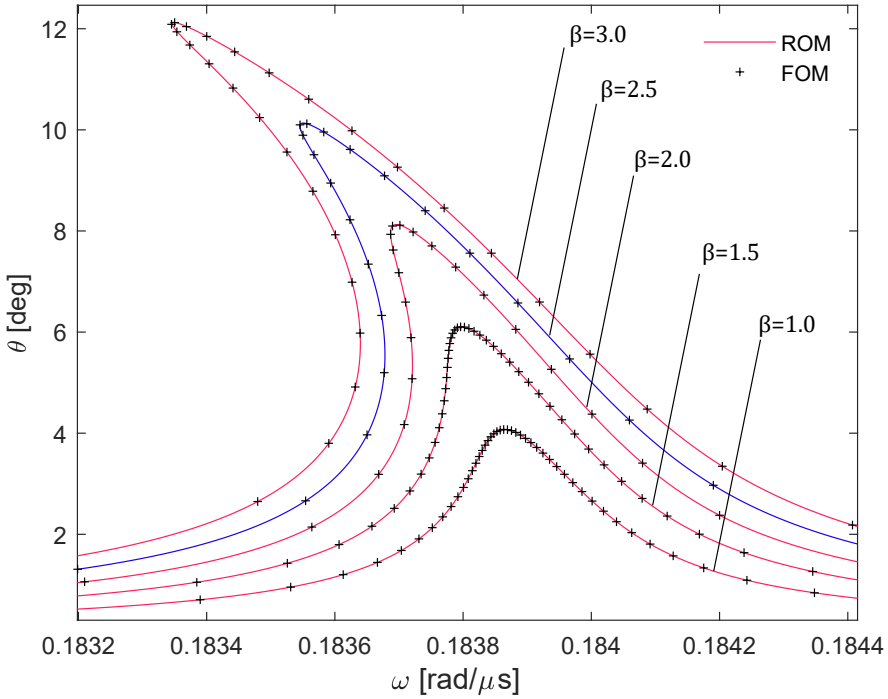

Figure 13: Micromirror 2: FRFs computed with the ROMs and 10 POMs compared with the FOM solution. The red continuous lines denote the test ROM solutions, while the blue one refers to the training data. The cross markers represent the FOM solutions

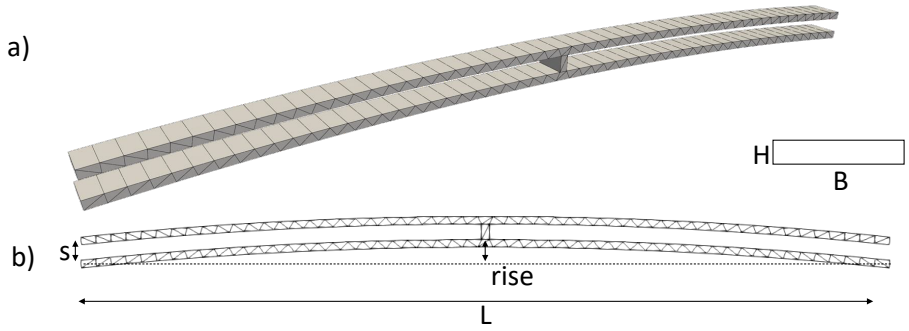

Figure 14: Shallow arch. Figure a): 3D view of the FEM model. Figure b): front view and main dimensions. $B = 20\,\mu$m, $H = 5\,\mu$m, $L = 530\,\mu$m, rise=13.4 μm, $s = 10\,\mu$m.

and able to represent the displacement field also for the fully coupled problem. This assumption is reasonable when the perturbation of the invariant manifold induced by the electrostatic couplings is moderate and will in general put an upper bound to the admissible EFs, i.e. on the bias voltages imposed on the electrodes. Since the electrostatic problem is quasi-static, the EFs depend only on the instantaneous values of the Q_i. This implies that, in a training stage, the $\mathbf{F}$ vector in Eq. (3) due to EFs can be computed with the FOM and projected on the POD subspace to generate $\mathbf{F}^{\mathrm{POD}}$ in Eq. (5) for any given combination of the weights Q_i of the POMs. The manifold of the electrostatic forces is thus pre-computed only at discrete points in preselected admissible ranges and is later interpolated between knots when queried during the integration of the ROM. Moreover, many POMs (like the "axial" POM in Figure 6 or high frequency bending POMs) have negligible effects on the EFs and can be disregarded so that EFs will depend on p_e electrically active POMs, with $p_e \ll p$ typically.

As a benchmark problem, we focus on a clamped-clamped beam meshed with quadratic elements and a total of 10920 nodes. The dimensions of the beam are $L = 1000\ \mu$m , $H = 10\ \mu$m , $B = 24\ \mu$m . An electrode is placed in front of the beam with a gap of $g = 5\ \mu$m and the voltage bias $V_{DC} + V_{AC}\cos\omega t$ is imposed between the electrode and the beam (see Figure 18a). The quality factor has been set to $Q = 10929$. The FOM utilized for the electrostatic problem is a Boundary Element Code (BEM) based on integral equations accelerated with Fast Multipoles and a total of 71844 unknowns. The code resorts to an iterative solver and its use in a fully coupled

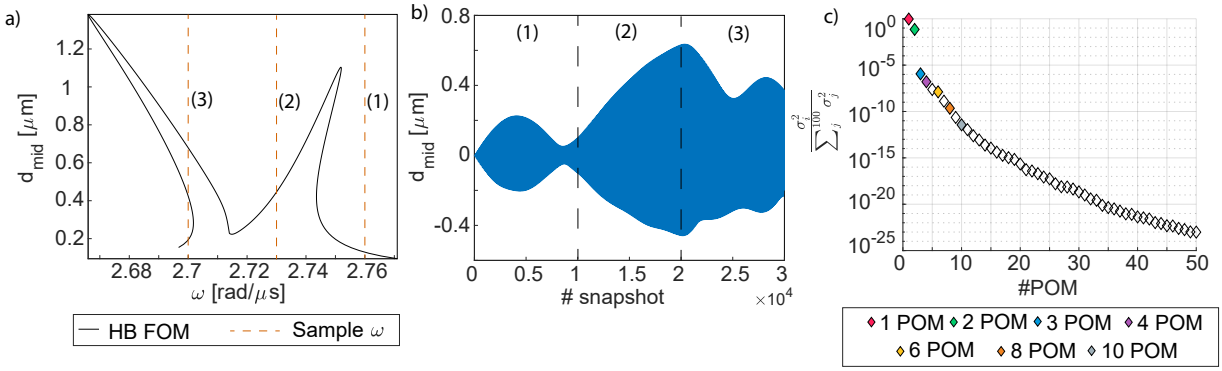

Figure 15: Snapshot set for the MEMS arch. Figure a): frequency points sampled with time marching methods represented as dashed lines superposed to the FOM FRF. Figure b): time history with the envelop of all the cycles simulated. Figure c): energy content of each POM.

solution would have a prohibitive cost.

The ROM is trained with mechanical HB-FEM simulations setting Q=10929 and applying a body load proportional to the first eigenmode $\mathbf{F}(t) = \mathbf{M}\boldsymbol{\phi}_1 \beta \cos(\omega t)$ with $\beta = 0.0005$. A total of 1850 snapshots have been collected on 37 sample frequencies identified by circles on the FOM solution of Figure 18b). The first 6 mechanical POMs, used to build the ROM, are depicted in Figure 18c).

Consistently with the previous assumptions we can consider that only the first POM will contribute significantly to EFs (i.e. $p_e = 1$). Thus, a series of electrostatic analyses are run imposing displacement fields proportional to the first POM $\mathbf{D} \approx \mathbf{U}_1 Q_1$ covering a range of $1.1\,\mu$m for the midspan displacement over a gap of $5\,\mu$m. The EFs are projected on the POMs yielding the equivalent forces expressed in μm. These forces are scaled by the applied potentials V_{DC} and V_{AC} and are modelled with a cubic polynomial as:

$$F_i^{\mathrm{POD}}(Q_1, V_{DC}, V_{AC}, \omega, t) = \left(V_{DC}^2 \epsilon_0 + 2 V_{DC} V_{AC} \epsilon_0 \cos(\omega t)\right) \left(\alpha_0^{(i)} + \alpha_1^{(i)} Q_1 + \alpha_2^{(i)} Q_1^2 + \alpha_3^{(i)} Q_1^3\right) \tag{7}$$

where $\alpha_j^{(i)}$ are coefficients of order j associated to the force projected on the i-th POM and ϵ_0 is the vacuum permittivity. In the example considered we neglect the components proportional to V_{AC}^2 (since typically $V_{AC} \ll V_{DC}$, see e.g. [7, 25]). The coefficients for the first 6 POMs are collected in Table 5.

POM	1	2	3	4	5	6
$\alpha_0^{(i)}$	6.8638	-0.9609	3.2838	1.9965	0.2274	2.5945
$\alpha_1^{(i)}$	0.0469	-0.0039	$2.86 \cdot 10^{-5}$	$-3.31 \cdot 10^{-5}$	0.0021	0.099
$\alpha_2^{(i)}$	$2 \cdot 10^{-4}$	$-1 \cdot 10^{-5}$	$-6 \cdot 10^{-5}$	$1 \cdot 10^{-5}$	$1 \cdot 10^{-5}$	$3 \cdot 10^{-4}$
$\alpha_3^{(i)}$	$1 \cdot 10^{-6}$	$-7 \cdot 10^{-8}$	$-5 \cdot 10^{-7}$	$1 \cdot 10^{-7}$	$5 \cdot 10^{-8}$	$1 \cdot 10^{-7}$

Table 5: Electromechanical problem: coefficients of the polynomial modeling Eq. (7)

In order to provide a validation of the ROM proposed we resort to the commercial software MEMS+ [84], which can perform electromechanical coupled simulations with structural elements. The model is built with 4 Timoshenko nonlinear beams with 4 nodes and the electrostatics is modelled with the method of conformal mappings. This simulation approach, though not general, is expected to be accurate for the simple MEMS tested.

Eigenmode	1	2	3	4	5
FEM model [kHz]	87.087	208.244	239.880	469.792	571.281
MEMS+ [kHz]	86.971	208.085	239.755	472.008	571.302

Table 6: Electromechanical problem: comparison between the eigenfrequencies given by the FEM model and MEMS+

We performed several simulations considering different combinations of V_{DC} and V_{AC} giving similar peak amplitudes: $V_{DC} = 1V$, $V_{AC} = 1V$; $V_{DC} = 20V$, $V_{AC} = 0.05V$; $V_{DC} = 40V$, $V_{AC} = 0.025V$; $V_{DC} = 60V$ and $V_{AC} = 0.0166V$.

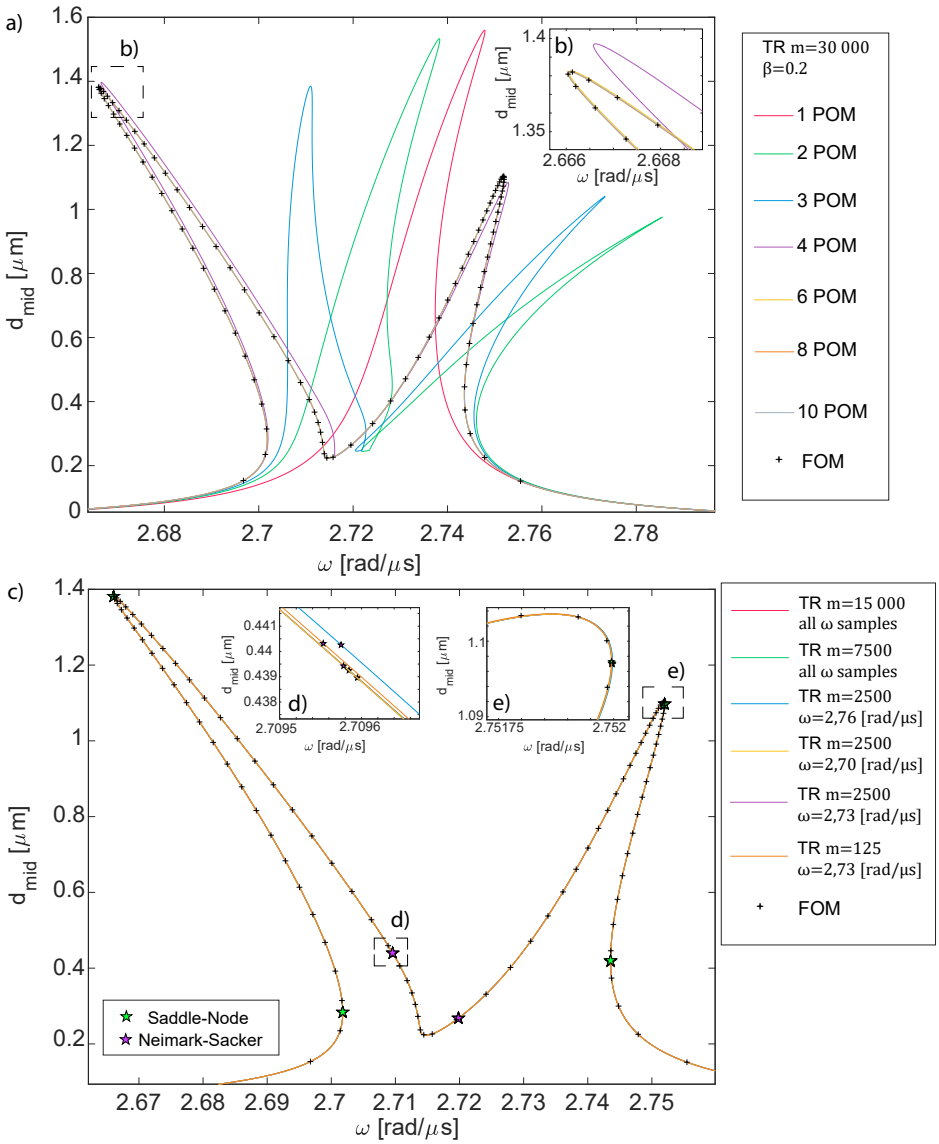

Figure 16: Convergence of the POD-ROM on the MEMS arch and dataset comparison. Figure a): FRFs resulting from each ROM built with a increasing number of POMs using the whole dataset. The POD is tested on the training set i.e., $\beta = 0.2$. Figure b) enlarged view of the resonance peak. Figure c) FRFs achieved with ROMS built on downsampled datasets. The POD ROM with 8 POMs is tested on the training set, i.e., $\beta = 0.2$. Figure d)-e) enlarged views of the resonance peak and of one Neimark-Sacker bifurcation point

The results are summarized in Figure 19a) collecting plots of the midspan deflection versus the actuation frequency. The curves are normalized with respect to the mechanical eigenfrequency of the lowest eigenmode. The FRFs display a shift of the resonant frequency towards the left induced by the expected electrostatic negative stiffness effect. The enlarged views in Figure 19b), 19c) and 19d) focus on specific frequency ranges for an improved comparison between the two classes of results. Another relevant effect induced by EFs is given by a softening contribution that mitigates the hardening of the response for increasing V_{DC}. To better highlight this latter effect, in Figure 19e) we superpose the various FRFs by filtering the mentioned shift and the static component of the displacement.

A very good agreement is achieved between the two simulation approaches concerning the shift and the overall nonlinearity evolution. However, as expected, for the largest values of V_{DC} a quantitative mismatch appears especially on the peak values. Indeed, as previously remarked, in the presence of large EFs the mechanical POMs might not guarantee an accurate representation of mechanical displacements. The fact that this disagreement occurs only at very large voltages unusual in MEMS application is however a strong validation of the proposed approach.

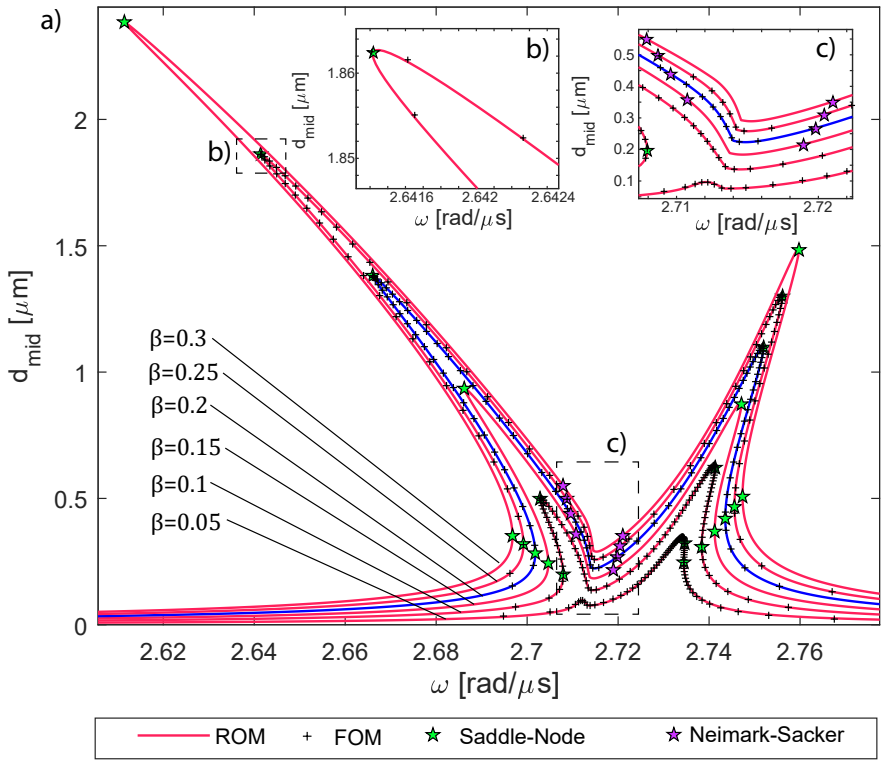

Figure 17: Shallow arch: FRFs computed with the ROM (8 POMs) compared with the FOM solutions. The red continuous lines are ROM solutions computed in the test phase, the blue one marking the training curve. The crosses denote the FOM solutions, while the star markers indicate the bifurcation points. The green and purple stars stand for Saddle-Node and Neimark-Sacker bifurcation points, respectively

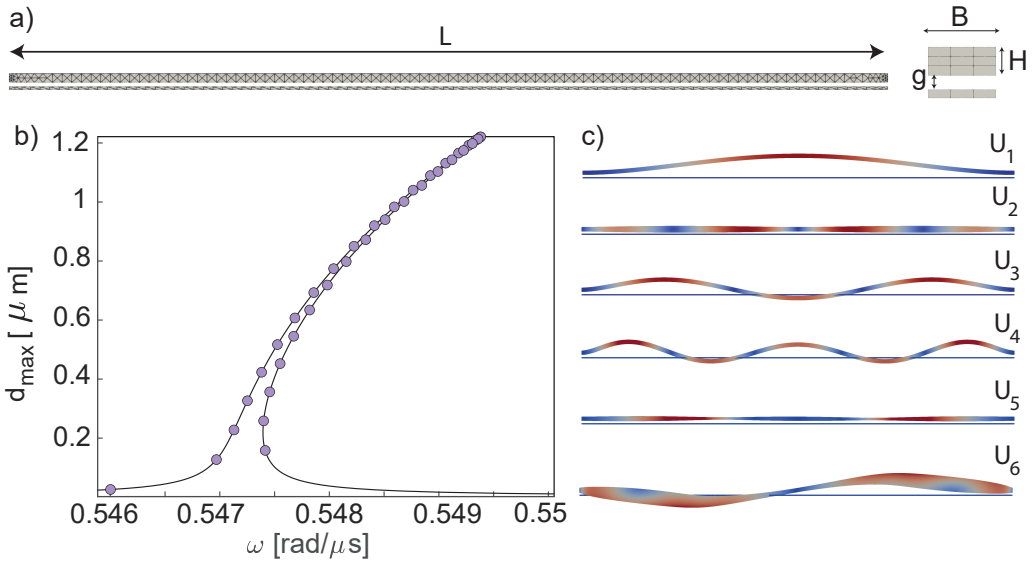

Figure 18: Electromechanical problem. Figure a) Clamped clamped beam used for electromechanical simulation side and front view. Figure b) FRF used as reference for the reduction. The frequency samples used to generate the POMs are marked with circles. Figure c) fist six POMs given by the FOM snapshots.

5 Conclusions

We have investigated various applications of POD-Galerkin ROMs for the sake of efficiently simulating MEMS devices. In particular, we have demonstrated how POD, despite being a *linear* reduction technique, can tackle very efficiently and accurately highly nonlinear features common in MEMS applications: large rotations, and

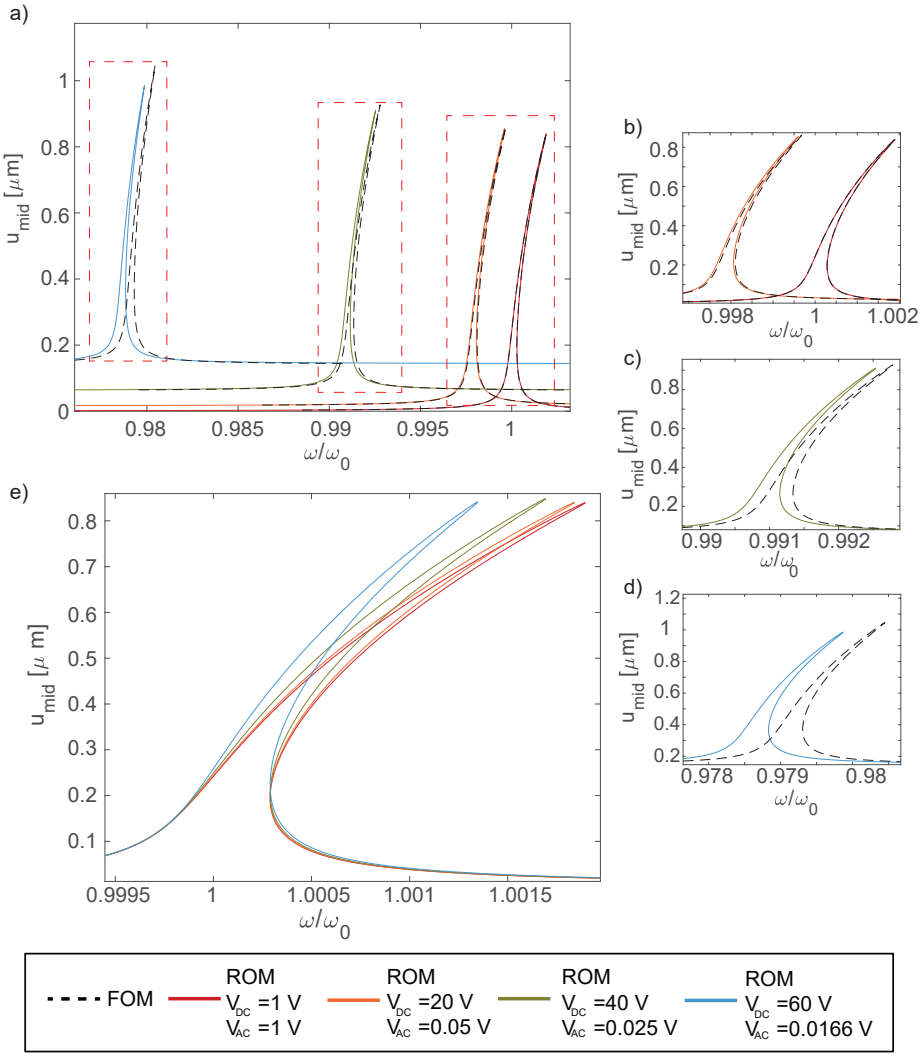

Figure 19: Electromechanical problem. Figure a): FRFs computed at four different voltage bias and comparison with the MEMS+ results. Figure b) c) d): enlarged views of the FRFs computed with the ROM. Figure e): FRFs superposed filtering the shift and showing the mitigation of the hardening effect

large geometrical transformations in general, internal resonances and electrostatic nonlinearities. Geometrical nonlinearities, leading to polynomial terms up to cubic order, have been reduced through an exact projection onto the subspace spanned by the POMs, while electrostatics has been modeled resorting to precomputed manifolds in terms of the amplitudes of the electrically active POMs.

We have tested extensively the reliability of the assumed linear trial space in challenging applications focusing on resonators, micromirrors and arches also displaying internal resonances. We have discussed several options to generate the matrix of snapshots using both classical time marching schemes and more advanced Harmonic Balance approaches. It has been shown that the method is robust and that a POD-Galerkin ROM can be trained also with transient time simulations far from steady state conditions. This might indeed be the only viable option in many applications, considering the cost and complexity of HB methods and the large quality factors typical of MEMS that prevent reaching steady state conditions with time-marching schemes.

In order to provide a deeper insight into the POD approach, we have also shown the similarity of the POMs extracted with the reconstruction vectors of the DNF approach that relies on the invariant manifold theory and verified that the trajectories predicted by the POD-Galerkin ROM perfectly lie on the manifolds of the DNF. This result further strengthens the interpretation of the POMs as the best linear approximation of the Nonlinear Normal Modes in the least square sense [51].

Another relevant feature of a POD-Galerkin ROM is that is allows to apply continuation methods and stability analysis of the dynamic solution, usually infeasible in FOM analyses. This provides the possibility to compute directly periodic solutions, trace the full FRF with both stable and unstable branches, and locate bifurcation

points by resorting to continuation codes available in the literature.

The whole set of challenging benchmarks developed seems to suggest a high potentiality, possibly so far underestimated, of the POD for this specific class of applications and stresses the reliability of the technique and its strong predictive ability.

Finally, a few conclusions and guidelines can be tentatively drafted. The dimension of the linear trial subspace has a lower bound that cannot be estimated a priori by considering only the oriented energy content. Usually the system dynamics is well modelled when the POMs retained in the basis reproduce the mappings predicted by the invariant manifold theory, i.e. DNF. This condition is hard to check but a strong connection between POMs and invariant manifold exists. This link guarantees that, when a proper number of POMs is used, the subspace correctly mimics the invariant manifold over which the system dynamics develops. Nevertheless, the minimum required dimension of the POD basis is always larger than that of the invariant manifold. When large transformations (e.g. large rotations) are involved, one needs to carefully tailor and check the POD subspace. In such conditions, the range of system parameters where the ROM can be safely used is reduced, as a consequence of the linearity of the trial space that cannot follow extreme changes in the solution. On the contrary, the technique seems to be highly robust with respect to the number of snapshots and to the type of FOM solver.

References

[1] G. Rega, H. Troger, Dimension reduction of dynamical systems: methods, models, applications, Nonlinear Dynamics 41 (1) (2005) 1–15.

[2] G. Kerschen, J.-C. Golinval, A. F. Vakakis, L. A. Bergman, The method of proper orthogonal decomposition for dynamical characterization and order reduction of mechanical systems: an overview, Nonlinear Dynamics 41 (1) (2005) 147–169.

[3] J. J. Hollkamp, R. W. Gordon, Reduced-order models for nonlinear response prediction: Implicit condensation and expansion, Journal of Sound and Vibration 318 (4-5) (2008) 1139–1153.

[4] M. P. Mignolet, A. Przekop, S. A. Rizzi, S. M. Spottswood, A review of indirect/non-intrusive reduced order modeling of nonlinear geometric structures, Journal of Sound and Vibration 332 (10) (2013) 2437–2460.

[5] C. Touzé, A. Vizzaccaro, O. Thomas, Model order reduction methods for geometrically nonlinear structures: a review of nonlinear techniques, Nonlinear Dynamics (2021) 1–50.

[6] A. Frangi, G. Gobat, Reduced order modelling of the non-linear stiffness in MEMS resonators, International Journal of Non-Linear Mechanics 116 (2019) 211–218.

[7] V. Zega, G. Gattere, S. Koppaka, A. Alter, G. D. Vukasin, A. Frangi, T. W. Kenny, Numerical modelling of non-linearities in MEMS resonators, Journal of Microelectromechanical Systems 29 (6) (2020) 1443–1454.

[8] A. Lazarus, O. Thomas, J.-F. Deü, Finite element reduced order models for nonlinear vibrations of piezoelectric layered beams with applications to NEMS, Finite Elements in Analysis and Design 49 (1) (2012) 35–51.

[9] A. H. Nayfeh, D. T. Mook, P. Holmes, Nonlinear oscillations (1980).

[10] A. H. Nayfeh, B. Balachandran, Modal interactions in dynamical and structural systems (1989).

[11] S. Krylov, B. R. Ilic, S. Lulinsky, Bistability of curved microbeams actuated by fringing electrostatic fields, Nonlinear Dynamics 66 (3) (2011) 403–426.

[12] D. A. Czaplewski, S. Strachan, O. Shoshani, S. W. Shaw, D. López, Bifurcation diagram and dynamic response of a MEMS resonator with a 1: 3 internal resonance, Applied Physics Letters 114 (25) (2019) 254104.

[13] S. Houri, D. Hatanaka, M. Asano, R. Ohta, H. Yamaguchi, Limit cycles and bifurcations in a nonlinear MEMS resonator with a 1: 3 internal resonance, Applied Physics Letters 114 (10) (2019) 103103.

[14] C. Van der Avoort, R. Van der Hout, J. Bontemps, P. Steeneken, K. Le Phan, R. Fey, J. Hulshof, J. Van Beek, Amplitude saturation of MEMS resonators explained by autoparametric resonance, Journal of Micromechanics and Microengineering 20 (10) (2010) 105012.

[15] L. Ruzziconi, N. Jaber, L. Kosuru, M. L. Bellaredj, M. I. Younis, Two-to-one internal resonance in the higher-order modes of a MEMS beam: Experimental investigation and theoretical analysis via local stability theory, International Journal of Non-Linear Mechanics 129 (2021) 103664.

[16] S. H. Nitzan, P. Taheri-Tehrani, M. Defoort, S. Sonmezoglu, D. A. Horsley, Countering the effects of nonlinearity in rate-integrating gyroscopes, IEEE Sensors Journal 16 (10) (2016) 3556–3563.

[17] A. Ganesan, C. Do, A. Seshia, Phononic frequency comb via intrinsic three-wave mixing, Physical Review Letters 118 (3) (2017) 033903.

[18] A. Ganesan, C. Do, A. Seshia, Phononic frequency comb via three-mode parametric resonance, Applied Physics Letters 112 (2) (2018) 021906.

[19] L. Xiong, L. Tang, B. R. Mace, Internal resonance with commensurability induced by an auxiliary oscillator for broadband energy harvesting, Applied Physics Letters 108 (20) (2016) 203901.

[20] T. Detroux, L. Renson, L. Masset, G. Kerschen, The harmonic balance method for bifurcation analysis of large-scale nonlinear mechanical systems, Computer Methods in Applied Mechanics and Engineering 296 (2015) 18–38.

[21] A. Opreni, N. Boni, R. Carminati, A. Frangi, Analysis of the nonlinear response of piezo-micromirrors with the harmonic balance method, in: Actuators, Vol. 10, MDPI, 2021, p. 21.

[22] A. A. Muravyov, S. A. Rizzi, Determination of nonlinear stiffness with application to random vibration of geometrically nonlinear structures, Computers & Structures 81 (15) (2003) 1513–1523.

[23] A. Givois, A. Grolet, O. Thomas, J.-F. Deü, On the frequency response computation of geometrically nonlinear flat structures using reduced-order finite element models, Nonlinear Dynamics 97 (2) (2019) 1747–1781.

[24] A. Vizzaccaro, A. Givois, P. Longobardi, Y. Shen, J.-F. Deü, L. Salles, C. Touzé, O. Thomas, Non-intrusive reduced order modelling for the dynamics of geometrically nonlinear flat structures using three-dimensional finite elements, Computational Mechanics 66 (6) (2020) 1293–1319.

[25] G. Gobat, V. Zega, P. Fedeli, L. Guerinoni, C. Touzé, A. Frangi, Reduced order modelling and experimental validation of a mems gyroscope test-structure exhibiting 1: 2 internal resonance, Scientific Reports 11 (1) (2021) 1–8.

[26] E. Nicolaidou, T. L. Hill, S. A. Neild, Indirect reduced-order modelling: using nonlinear manifolds to conserve kinetic energy, Proceedings of the Royal Society A 476 (2243) (2020) 20200589.

[27] G. Haller, S. Ponsioen, Exact model reduction by a slow–fast decomposition of nonlinear mechanical systems, Nonlinear Dynamics 90 (1) (2017) 617–647.

[28] Y. Shen, N. Béreux, A. Frangi, C. Touzé, Reduced order models for geometrically nonlinear structures: Assessment of implicit condensation in comparison with invariant manifold approach, European Journal of Mechanics-A/Solids 86 (2021) 104165.

[29] Y. Shen, A. Vizzaccaro, N. Kesmia, T. Yu, L. Salles, O. Thomas, C. Touzé, Comparison of reduction methods for finite element geometrically nonlinear beam structures, Vibration 4 (1) (2021) 175–204.

[30] A. Quarteroni, A. Manzoni, F. Negri, Reduced basis methods for partial differential equations: an introduction, Vol. 92, Springer, 2015.

[31] K. Lu, Y. Jin, Y. Chen, Y. Yang, L. Hou, Z. Zhang, Z. Li, C. Fu, Review for order reduction based on proper orthogonal decomposition and outlooks of applications in mechanical systems, Mechanical Systems and Signal Processing 123 (2019) 264–297.

[32] M. Amabili, A. Sarkar, M. Païdoussis, Chaotic vibrations of circular cylindrical shells: Galerkin versus reduced-order models via the proper orthogonal decomposition method, Journal of Sound and Vibration 290 (3-5) (2006) 736–762.

[33] M. Amabili, A. Sarkar, M. Paıdoussis, Reduced-order models for nonlinear vibrations of cylindrical shells via the proper orthogonal decomposition method, Journal of Fluids and Structures 18 (2) (2003) 227–250.

[34] O. Weeger, U. Wever, B. Simeon, On the use of modal derivatives for nonlinear model order reduction, International Journal for Numerical Methods in Engineering 108 (13) (2016) 1579–1602.

[35] S. Jain, P. Tiso, J. B. Rutzmoser, D. J. Rixen, A quadratic manifold for model order reduction of nonlinear structural dynamics, Computers & Structures 188 (2017) 80–94.

[36] J. B. Rutzmoser, D. J. Rixen, P. Tiso, S. Jain, Generalization of quadratic manifolds for reduced order modeling of nonlinear structural dynamics, Computers & Structures 192 (2017) 196–209.

[37] M. K. Mahdiabadi, P. Tiso, A. Brandt, D. J. Rixen, A non-intrusive model-order reduction of geometrically nonlinear structural dynamics using modal derivatives, Mechanical Systems and Signal Processing 147 (2021) 107126.

[38] A. Vizzaccaro, L. Salles, C. Touzé, Comparison of nonlinear mappings for reduced-order modelling of vibrating structures: normal form theory and quadratic manifold method with modal derivatives, Nonlinear Dynamics 103 (4) (2021) 3335–3370.

[39] R. M. Rosenberg, The normal modes of nonlinear n-degree-of-freedom systems (1962).

[40] S. Shaw, An invariant manifold approach to nonlinear normal modes of oscillation, Journal of Nonlinear Science 4 (1) (1994) 419–448.

[41] C. Touzé, O. Thomas, A. Chaigne, Hardening/softening behaviour in non-linear oscillations of structural systems using non-linear normal modes, Journal of Sound and Vibration 273 (1-2) (2004) 77–101.

[42] C. Touzé, M. Amabili, Nonlinear normal modes for damped geometrically nonlinear systems: Application to reduced-order modelling of harmonically forced structures, Journal of Sound and Vibration 298 (4-5) (2006) 958–981.

[43] C. Touzé, Normal form theory and nonlinear normal modes: theoretical settings and applications, in: Modal analysis of nonlinear mechanical systems, Springer, 2014, pp. 75–160.

[44] G. Haller, S. Ponsioen, Nonlinear normal modes and spectral submanifolds: existence, uniqueness and use in model reduction, Nonlinear Dynamics 86 (3) (2016) 1493–1534.

[45] S. Ponsioen, T. Pedergnana, G. Haller, Automated computation of autonomous spectral submanifolds for nonlinear modal analysis, Journal of Sound and Vibration 420 (2018) 269–295.

[46] L. Renson, G. Kerschen, B. Cochelin, Numerical computation of nonlinear normal modes in mechanical engineering, Journal of Sound and Vibration 364 (2016) 177–206.

[47] A. Vizzaccaro, Y. Shen, L. Salles, J. Blahoš, C. Touzé, Direct computation of nonlinear mapping via normal form for reduced-order models of finite element nonlinear structures, Computer Methods in Applied Mechanics and Engineering 384 (2021) 113957.

[48] A. Opreni, A. Vizzaccaro, A. Frangi, C. Touzé, Model Order Reduction based on Direct Normal Form: Application to Large Finite Element MEMS Structures Featuring Internal Resonance, Nonlinear Dynamics 105 (2021) 1237 – 1272.

[49] G. Kerschen, J.-C. Golinval, Physical interpretation of the proper orthogonal modes using the singular value decomposition, Journal of Sound and Vibration 249 (5) (2002) 849–865.

[50] R. Sampaio, C. Soize, Remarks on the efficiency of POD for model reduction in non-linear dynamics of continuous elastic systems, International Journal for Numerical Methods in Engineering 72 (1) (2007) 22–45.

[51] M. Amabili, C. Touzé, Reduced-order models for nonlinear vibrations of fluid-filled circular cylindrical shells: comparison of POD and asymptotic nonlinear normal modes methods, Journal of Fluids and Structures 23 (6) (2007) 885–903.

[52] P. Tiso, D. J. Rixen, Reduction methods for MEMS nonlinear dynamic analysis, in: Nonlinear Modeling and Applications, Volume 2, Springer, 2011, pp. 53–65.

[53] J. S. Han, E. B. Rudnyi, J. G. Korvink, Efficient optimization of transient dynamic problems in MEMS devices using model order reduction, Journal of Micromechanics and Microengineering 15 (4) (2005) 822.

[54] L. E. Malvern, Introduction to the Mechanics of a Continuous Medium, no. Monograph, 1969.

[55] M. Barrault, Y. Maday, N. C. Nguyen, A. T. Patera, An 'empirical interpolation' method: Application to efficient reduced-basis discretization of partial differential equations, Comptes Rendus Mathématique de l'Académie des Sciences 339 (9) (2004) 667–672.

[56] S. Chaturantabut, D. C. Sorensen, Nonlinear model reduction via discrete empirical interpolation, SIAM Journal on Scientific Computing 32 (5) (2010) 2737–2764.

[57] Y. Maday, N. Nguyen, A. Patera, G. Pau, A general multipurpose interpolation procedure: The magic points, Communications on Pure and Applied Analysis 8 (2008) 383–404.

[58] E. J. Doedel, A. R. Champneys, F. Dercole, T. F. Fairgrieve, Y. A. Kuznetsov, B. Oldeman, R. Paffenroth, B. Sandstede, X. Wang, C. Zhang, AUTO-07P: Continuation and bifurcation software for ordinary differential equations (2007).

[59] L. Guillot, B. Cochelin, C. Vergez, A Taylor series-based continuation method for solutions of dynamical systems, Nonlinear Dynamics 98 (4) (2019) 2827–2845.

[60] L. Guillot, A. Lazarus, O. Thomas, C. Vergez, B. Cochelin, A purely frequency based Floquet-Hill formulation for the efficient stability computation of periodic solutions of ordinary differential systems, Journal of Computational Physics 416 (2020) 109477.

[61] M. Krack, J. Gross, Harmonic balance for nonlinear vibration problems, Vol. 1, Springer, 2019.

[62] H. Dankowicz, F. Schilder, Recipes for continuation, SIAM, 2013.

[63] R. Veltz, BifurcationKit.jl (Jul. 2020).
URL `https://hal.archives-ouvertes.fr/hal-02902346`

[64] B. Cochelin, C. Vergez, A high order purely frequency-based harmonic balance formulation for continuation of periodic solutions, Journal of Sound and Vibration 324 (1-2) (2009) 243–262.

[65] G. Buza, S. Jain, G. Haller, Using spectral submanifolds for optimal mode selection in nonlinear model reduction, Proceedings of the Royal Society A 477 (2246) (2021) 20200725.

[66] X. Cabré, E. Fontich, R. De La Llave, The parameterization method for invariant manifolds III: overview and applications, Journal of Differential Equations 218 (2) (2005) 444–515.

[67] A. Haro, R. de la Llave, A parameterization method for the computation of invariant tori and their whiskers in quasi-periodic maps: numerical algorithms, Discrete & Continuous Dynamical Systems-B 6 (6) (2006) 1261.

[68] A. Haro, R. de la Llave, A parameterization method for the computation of invariant tori and their whiskers in quasi-periodic maps: rigorous results, Journal of Differential Equations 228 (2) (2006) 530–579.

[69] A. Haro, M. Canadell, J.-L. Figueras, A. Luque, J.-M. Mondelo, The parameterization method for invariant manifolds, Applied Mathematical Sciences 195 (2016).

[70] S. Jain, G. Haller, How to compute invariant manifolds and their reduced dynamics in high-dimensional finite-element models?, arXiv preprint arXiv:2103.10264 (2021).

[71] A. Vizzaccaro, A. Opreni, L. Salles, A. Frangi, C. Touzé, High order direct parametrisation of invariant manifolds for model order reduction of finite element structures: application to large amplitude vibrations and uncovering of a folding point, arXiv preprint arXiv:2109.10031 (2021).

[72] S. Shaw, C. Pierre, Non-linear normal modes and invariant manifolds, Journal of sound and Vibration 150 (1) (1991) 170–173.

[73] A. Corigliano, B. De Masi, A. Frangi, C. Comi, A. Villa, M. Marchi, Mechanical characterization of polysilicon through on-chip tensile tests, Journal of Microelectromechanical Systems 13 (2) (2004) 200–219.

[74] Laser beam scanning, `https://www.st.com/content/st_com/en/about/innovation---technology/laser-beam-scanning.html`.

[75] A. Frangi, A. Opreni, N. Boni, P. Fedeli, R. Carminati, M. Merli, G. Mendicino, Nonlinear response of PZT-actuated resonant micromirrors, Journal of Microelectromechanical Systems 29 (6) (2020) 1421–1430.

[76] M. A. Hopcroft, W. D. Nix, T. W. Kenny, What is the Young's modulus of silicon?, Journal of Microelectromechanical Systems 19 (2) (2010) 229–238.

[77] G. Gobat, L. Guillot, A. Frangi, B. Cochelin, C. Touzé, Backbone curves, Neimark-Sacker boundaries and appearance of quasi-periodicity in nonlinear oscillators: application to 1: 2 internal resonance and frequency combs in MEMS, Meccanica (2021) 1–33.

[78] A. Frangi, B. De Masi, F. Confalonieri, S. Zerbini, Threshold shock sensor based on a bistable mechanism: design, modeling, and measurements, Journal of Microelectromechanical Systems 24 (6) (2015) 2019–2026.

[79] W. N. Sharpe, B. Yuan, R. Vaidyanathan, R. L. Edwards, Measurements of Young's modulus, Poisson's ratio, and tensile strength of polysilicon, in: Proceedings IEEE the tenth annual international workshop on micro electro mechanical systems. An investigation of micro structures, sensors, actuators, machines and robots, IEEE, 1997, pp. 424–429.

[80] M. I. Younis, E. M. Abdel-Rahman, A. Nayfeh, A reduced-order model for electrically actuated microbeam-based MEMS, Journal of Microelectromechanical Systems 12 (5) (2003) 672–680.

[81] M. I. Younis, A. Nayfeh, A study of the nonlinear response of a resonant microbeam to an electric actuation, Nonlinear Dynamics 31 (1) (2003) 91–117.

[82] M. Barrault, Y. Maday, N. C. Nguyen, A. T. Patera, An ' empirical interpolation ' method: application to efficient reduced-basis discretization of partial differential equations, Comptes Rendus Mathematique 339 (9) (2004) 667–672.

[83] S. L. Brunton, J. N. Kutz, Data-driven science and engineering: Machine learning, dynamical systems, and control, Cambridge University Press, 2019.

[84] J. Nazdrowicz, A. Napieralski, Modelling, simulations and performance analysis of MEMS vibrating gyroscope in coventor MEMS+ environment, in: 2019 20th International Conference on Thermal, Mechanical and Multi-Physics Simulation and Experiments in Microelectronics and Microsystems (EuroSimE), IEEE, 2019, pp. 1–5.

A Analysis of computational performances

In this Appendix we discuss the computational performances of the FOM and of the offline-online stages of the ROM for the mechanical examples of Section 3. These data further stress the efficiency of the ROM and provide the trend of the achieved speed-up.

The comparison between the cost of the FOM and of the online stage of the ROM is reported in Table 7, while an analysis of the offline stage is reported in Table 8. All the simulations have been run on a workstation with AMD Ryzen 5 1600 Six-Core Processor 3.20 GHz with 64 GB RAM. For HB methods the computational time only includes the calculation of the harmonic components and it does not account for the reconstruction of the time history over the period, while for time-marching methods the cost of all the steps of the time history is provided.

Application	FOM-m	T_{FOM} [10^6 s]	p	$T_{\text{online}}[s]$	$T_{\text{FOM}}/T_{\text{online}}$
C-C Beam	HB (9)	0.21	6	42	5023
C-C Beam	TM-SS (50)	1.35	6	42	32143
Micromirror 1	HB (5)	0.44	8	452	969
Micromirror 2	HB (7)	0.2	10	220	918
Arch	HB (9)	0.12	8	250	480
Arch	TM-SS (50)	9	8	250	36000

Table 7: Cost of the FOM and of the online stage of the ROM considering 1000 frequency instances for a fixed forcing level

In Table 7 the FOM-m column specifies the solution technique used for the full order model according to the conventions introduced in Section 3. Within brackets we provide the number of time steps in one period for

time marching methods (TM) or the number of harmonic components for HB methods. T_{FOM} is the average computing time required to obtain a FOM solution for 1000 frequencies and a single forcing level, which is equivalent to a finely sampled FRF with continuation methods. The p column provides the number of POMs used in the reduction. T_{online} is the average time required to compute the ROM solution for 1000 frequencies and a single forcing level. The last column provides the speed-up defined in this case as the ration between T_{FOM} and T_{online}. Indeed, when the offline cost is not an issue and one is mainly interested in the online phase, this is the most important performance indicator. One comment is worth stressing concerning the FOM solved with time marching methods. It appears that the time marching approach is not suitable for MEMS applications when the steady state regime is needed, as is the case herein. Indeed this is due to the large quality factors Q typical of MEMS. For the C-C beam and the arch resonator we consider that the steady state is reached after $6Q$ periods and, despite the fact that the Q factors considered are unrealistically small, the computing cost explodes.

Application	FOM-m	$\#\omega$	m	$T_{\text{snap}}[s]$	$T_{\text{offline}}[s]$	$\frac{T_{\text{FOM}}}{T_{\text{online}}+T_{\text{offline}}}$
C-C Beam	HB (9)	10	500	2110	2 301	90
C-C Beam	TM-SS (100)	2	1242	720	770	259
C-C Beam	TM-SS (100)	10	6210	3600	4014	52
C-C Beam	TM-SS (100)	20	12420	7200	8206	25
C-C Beam	TM-TR (100)	1	1000	90	137	1178
Micromirror 1	HB (5)	50	5000	3026	25526	16
Micromirror 2	HB (7)	40	2000	8080	16410	12
Arch	TM (100)	3	30000	1800	3530	31

Table 8: Analysis of the offline stage

In Table 8 we focus on the contrary on the offline stage and provide a second possible measure of speed-up. As before, the FOM-m column specifies the solution technique utilized for the full order model and the number within brackets gives the number of time steps in one period for time marching methods (TM) or the number of harmonic components for HB methods. $\#\omega$ is the number of frequency instances used in the training and m is the total number of snapshots used in the SVD (including both frequency and forcing variations). The T_{snap} column provides the time required to compute the snapshots with the FOM. T_{offline} is the sum of T_{snap}, of the time required to perform the SVD decomposition (package used ARPACK in `FORTRAN`) and of the cost of the projection onto the ROM subspace. Finally we report a second possible speed-up measure $T_{\text{FOM}}/(T_{\text{online}} + T_{\text{offline}})$ that includes also the impact of T_{offline}. The T_{FOM} and the T_{online} are the one in Table 7, HB method is considered in T_{FOM}. This alternative speed measure, shows that T_{offline} represents a significant part of the computational effort, nevertheless the ROM is still convenient. The time spent in the offline stage may overcome the gain achieved in the online stage when few parameter queries are simulated with the ROM. However in MEMS applications, considering all the features mentioned in this work (e.g high Q factor, large models, multiple parameters to span etc.) the computation gain is always much greater than 1.

Let us consider the C-C beam case where we compare the offline cost of four different conditions: HB FOM, 5,10 and 20 frequency samples with snapshots taken close to steady state (SS, see Figure 5a) and one frequency with transient time series (TR, see Figure 5b)) generated with TM methods. This highlights that TM methods represent an appealing alternative as a limited number of snapshots sampled in a fully transient state still allows to identify a proper subspace, as pointed out in Section 3.1.

MOX Technical Reports, last issues

Dipartimento di Matematica
Politecnico di Milano, Via Bonardi 9 - 20133 Milano (Italy)

06/2022 Pozzi, G.; Grammatica, B.; Chaabane, L.; Catucci, M.; Mondino, A.; Zunino, P.; Ciarletta, P.
T cell therapy against cancer: a predictive diffuse-interface mathematical model informed by pre-clinical studies

07/2022 Sinigaglia, C.; Quadrelli, D.E.; Manzoni, A.; Braghin, F.
Fast active thermal cloaking through PDE-constrained optimization and reduced-order modeling

05/2022 Aspri, A; Beretta, E.; Cavaterra, C.; Rocca, E.; Verani, M.
Identification of cavities and inclusions in linear elasticity with a phase-field approach

04/2022 Africa, P.C.; Piersanti, R.; Fedele, M.; Dede', L.; Quarteroni, A.
lifex - heart module: a high-performance simulator for the cardiac function

02/2022 Antonietti, P.F.; Scacchi, S.; Vacca, G.; Verani, M.
C^1-VEM for some variants of the Cahn-Hilliard equation: a numerical exploration

03/2022 Giacomini, M.; Perotto, S.
Anisotropic mesh adaptation for region-based segmentation accounting for image spatial information

01/2022 Gavazzoni, M.; Ferro, N.; Perotto, S.; Foletti, S.
Multi-physics inverse homogenization for the design of innovative cellular materials: application to thermo-mechanical problems

95/2021 Di Gregorio, S.; Vergara, C.; Montino Pelagi, G.; Baggiano, A.; Zunino, P.; Guglielmo, M.; Fu
Prediction of myocardial blood flow under stress conditions by means of a computational model

92/2021 Antonietti, P.F.; Manzini, G.; Scacchi, S.; Verani, M.
On arbitrarily regular conforming virtual element methods for elliptic partial differential equations

94/2021 Antonietti, P.F.; Berrone, S.; Busetto, M.; Verani, M.
Agglomeration-based geometric multigrid schemes for the Virtual Element Method